1-1-2016

Regional Mechanical Properties and Microstructure of Ovine Heart Chambers

Shahnaz Javani
University of Denver

Regional Mechanical Properties and Microstructure of Ovine Heart Chambers

Abstract

Mechanical properties of cardiac tissue play an important role in the normal heart function. As a baseline for understanding of physiology and pathophysiology of the heart, and for development and validation of new therapies, it is crucial to first understand the mechanical behavior of the normal heart tissue. Although heart chambers have the same embryonic origin, differences in the development of mechanical properties are expected to manifest over time during the adulthood period. Therefore, the goal of this study was to determine the passive mechanical properties of all heart chambers through a paired comparison study in an ovine model. Ovine heart was used due its physiological and anatomical similarities to human heart. A total of 189 specimens from anterior and posterior portions of the left and right ventricles, atria, and appendages underwent biaxial mechanical testing. A Fung-type strain energy function was used to fit the experimental data. Tissue behavior was quantified based on the magnitude of strain energy, as an indicator of tissue stiffness, at equibiaxial strains of 0.10, 0.15, and 0.20. Statistical analysis revealed no significant difference in strain energy storage between anterior and posterior portions of each chamber, except for the right ventricle where strain energy storage in the posterior specimens were higher than the anterior specimens. Additionally, all chambers from the left side of the heart had significantly higher strain energy storage than the corresponding chambers on the right side. Furthermore, the highest to lowest stored strain energy were associated with ventricles, appendages, and atria, respectively. Microstructure of tissue specimens from different chambers was also compared using histology. The average surface area ratio of collagen to myocyte was found to be highest for the atria and lowest for the ventricles. This fact could explain the underlying basis for the differences in tissue stiffness between the regions.

Document Type

Thesis

Degree Name

M.S.

Department

Mechanical Engineering

First Advisor

Ali N. Azadani, Ph.D.

Second Advisor

Peter Laz

Third Advisor

Yun Bo Yi

Keywords

Atrial appendage, Biaxial testing, Cardiac mechanics, Microstructure, Passive mechanical behavior, Ventricle, Atrium

Subject Categories

Biomedical Engineering and Bioengineering

REGIONAL MECHANICAL PROPERTIES AND MICROSTRUCTURE OF OVINE HEART CHAMBERS

A Thesis

Presented to

the Faculty of the Daniel Felix Ritchie School of Engineering and Computer Science

University of Denver

In Partial Fulfillment

of the Requirements for the Degree

Master of Science

by

Shahnaz Javani

November 2016

Advisor: Ali N. Azadani

Author: Shahnaz Javani
Title: REGIONAL MECHANICAL PROPERTIES AND MICROSTRUCTURE OF OVINE HEART CHAMBERS
Advisor: Ali N. Azadani
Degree Date: November 2016

ABSTRACT

Mechanical properties of cardiac tissue play an important role in the normal heart function. As a baseline for understanding of physiology and pathophysiology of the heart, and for development and validation of new therapies, it is crucial to first understand the mechanical behavior of the normal heart tissue. Although heart chambers have the same embryonic origin, differences in the development of mechanical properties are expected to manifest over time during the adulthood period. Therefore, the goal of this study was to determine the passive mechanical properties of all heart chambers through a paired comparison study in an ovine model. Ovine heart was used due its physiological and anatomical similarities to human heart. A total of 189 specimens from anterior and posterior portions of the left and right ventricles, atria, and appendages underwent biaxial mechanical testing. A Fung-type strain energy function was used to fit the experimental data. Tissue behavior was quantified based on the magnitude of strain energy, as an indicator of tissue stiffness, at equibiaxial strains of 0.10, 0.15, and 0.20. Statistical analysis revealed no significant difference in strain energy storage between anterior and posterior portions of each chamber, except for the right ventricle where strain energy storage in the posterior specimens were higher than the anterior specimens. Additionally, all chambers from the left side of the heart had significantly higher strain energy storage than the corresponding chambers on the right side. Furthermore, the highest to lowest stored strain energy were associated with ventricles, appendages, and atria, respectively. Microstructure of tissue specimens from different chambers was also compared using histology.

TABLE OF CONTENTS

LIST OF TABLES

LIST OF FIGURES

CHAPTER 1: INTRODUCTION

The heart is the first organ to function during embryonic development. It starts to function during the fourth week when the delivery of nutrients and removal of wastes can no longer be met by diffusion from the placenta. The remodeling of the heart from the primitive heart tube to the formation of the mature four-chambered heart by looping and septation has been studied for over a century[19] (Figure 1.1). Shortly after the onset of looping, the ventricular and atrial chambers are formed within the heart tube. Then, the common atrium is arranged through septation into right and left atria, and the ventricle is separated by the interventricular septum into two chambers. Furthermore, differentiation and proliferation at the venous pole of the heart tube results in the formation of the atrial appendages[26]. Although heart chambers have the same embryonic origin, differences in the development of mechanical properties are expected to manifest over time during the adulthood period.

Mechanical properties of heart chambers play an important role in cardiac function and heart physiology. It is well known that the mechanical state of the heart considerably influence cardiomyocyte electrophysiology through a process known as mechano-electric coupling[21]. The mechano-electric coupling involves both feed-forward connection between electrical excitation and mechanical contraction[4], as well as feed-backward connection from the mechanical environment to initiation and spread of cardiac excitation, also known as the mechano-electric feedback[13]. The mechano-electric coupling is essential for normal heart function. Disease-related alterations in heart mechanical properties may contribute to electrophysiological changes

responsible for cardiac arrhythmias, such as ventricular tachyarrhythmias and atrial fibrillation. The high incidence of sudden cardiac death following myocardial infarction is believed to relate to ventricular fibrillation induced by electrophysiological alterations in the border zone of the infarct[22]. Therefore, mechanics and electrophysiology are interlinked and greater knowledge of the passive mechanical properties of different anatomical regions of the heart is important to accurately understand and characterize the mechano-electric coupling mechanism of the entire heart.

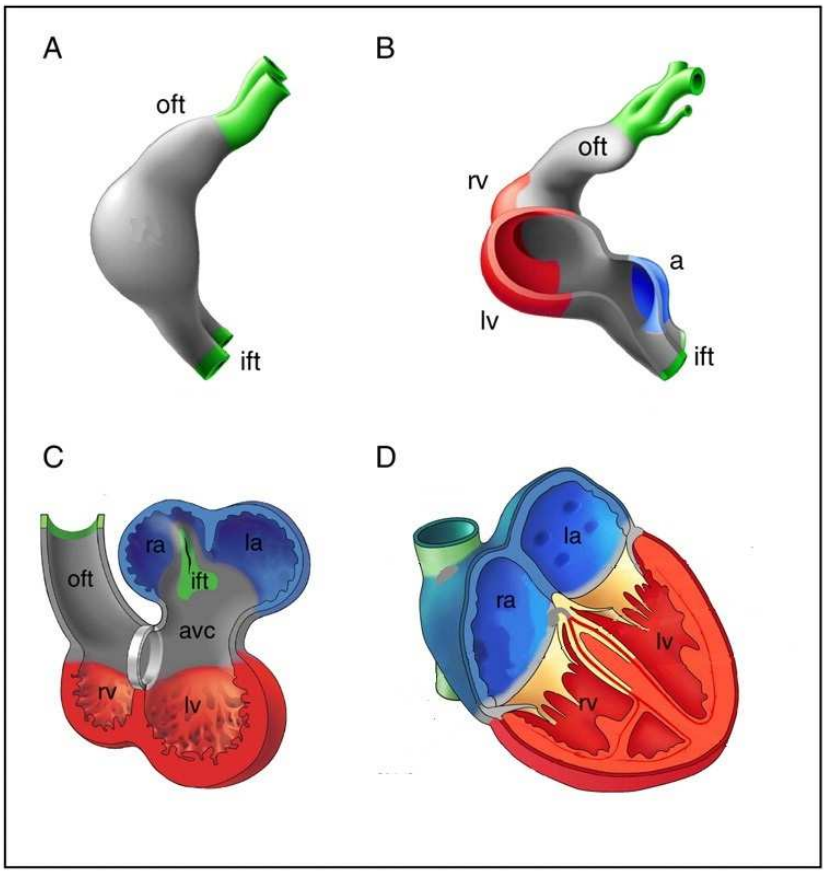

Figure 1.1: Heart development from primary heart tube to the mature heart. Components in the forming heart (A-C) can be tracked to the mature heart (D). Oft, outflow track; ift, inflow track; rv, right ventricle; lv, left ventricle; a, atrium; ra, right atrium; la, left atrium; avc, atrioventricular canal[30].

In addition, more comprehensive data on mechanical properties of normal heart is required for design and evaluation of treatment options for cardiovascular diseases, such as

myocardial infarction and heart failure. Infarct expansion which occurs within hours of myocardial infarction is the result of wall thinning and ventricular dilation. Previous studies suggest restraining infarct expansion to normalize left ventricular geometry by use of surgical ventricular restoration techniques[16] or by injection of polymer-based biomaterials into ventricular wall[15]. Furthermore, recent studies suggest modification of infarct material properties by implantation of tissue engineered patches over the infarcted cardiac tissue to attenuate the post-infarction remodeling[28]. Matching the mechanical properties of the matrix material with myocardium would allow efficient mechanical signal transfer from the myocardial environment to the tissue engineered cardiac grafts. Therefore, it is important to design engineered cardiac patches that match the mechanical properties of the native myocardium[29].

Moreover, heart failure is a highly prevalent disorder that is associated with considerable morbidity and mortality. An increase in the left ventricular wall stress during pressure overload due to hypertension or valvular heart disease is hypothesized to lead to compensatory hypertrophy[7]. In the case of pathological cardiac hypertrophy, the process translates into eventual heart failure. Furthermore, the right ventricle can be affected by a number of diseases most notably pulmonary hypertension. The adaptive response of right ventricle is followed by progressive contractile dysfunction, dilation, and eventually heart failure[27]. Since ventricular wall stress affects ventricular remodeling, normalization of ventricular wall stress is the cornerstone of many existing and new treatment options for heart failure[6]. Therefore, further understanding of structure and mechanical properties of left and right ventricles is necessary to optimize heart failure treatment options[6].

Similar to the ventricles, local mechanical characterization of the atria is important to characterize normal propagation of electrical impulses in the atrial chambers. Alteration in the normal propagation of the impulses may contribute to the onset and progression of cardiac

arrhythmias such as atrial fibrillation. Atrial fibrillation is the most common sustained arrhythmia encountered in clinical practice that highly increases the risk of stroke. Although a complete understanding of the fundamental mechanisms responsible for atrial fibrillation has not been established, synergistic contribution of electrophysiological, biochemical, and mechanical remodeling was proven to mediate development of atrial fibrillation[14]. In addition, assessment of the mechanical behavior of the atria and atrial appendages is necessary to determine the interaction between tissue and implantable medical devices such as atrial appendage and septal defect closure devices.

Thus, understanding the complex tissue structure and mechanical behavior of heart chambers has been the subject of many studies. However, majority of the studies were focused on a single heart chamber rather than the entire heart. There is a need for further fundamental research to obtain more information about the structure and mechanical properties of all heart chambers to better understand heart physiology and pathophysiology, and validate treatment options for cardiovascular diseases. The goal of the present work was to determine passive mechanical properties and microstructure of all heart chambers through a paired comparison study in an ovine model. Biaxial stretch tests were performed on excised samples obtained from different anatomical regions of healthy ovine hearts, namely right and left ventricles, atria, and appendages. The rationale for using sheep heart was its documented physiological, functional, and anatomical similarities to human heart, as well as its lack of collateral coronary circulation that has made it a widely used animal model in the studies of myocardial infarction and heart failure[10, 11]. To the best of our knowledge, this is the first study to compare mechanical behavior and microstructure of heart chambers through a paired comparison approach.

CHAPTER 2: ANATOMY AND PHYSIOLOGY OF HUMAN HEART

The heart is a muscular organ a little larger than the size of a closed fist that functions as the body's circulatory pump. It is located in the thoracic cavity medial to the lungs and posterior to the sternum. The base of the heart is attached to the aorta, pulmonary arteries, pulmonary veins, and the vena cava, and is located along the body's midline. The tip of the heart, known as apex, points toward the left side of the body, and rests just superior to the diaphragm.

The heart sits within a fluid-filled cavity called pericardial cavity, which consists of a double-layered membrane called pericardium. The inner layer of the pericardium, called the visceral layer, covers the outside of the heart, and the outer layer called parietal layer forms a sac around the outside of the pericardial cavity (Figure 2.1). The parietal layer surrounds the roots of the heart's major blood vessels and is attached by ligaments to the spinal column, diaphragm, and other parts of the body. A coating of fluid separates the two layers allowing normal heart movement within the chest. Pericardium serves two functions; it produces serous fluid to lubricate the heart and prevent friction between the heart and the surrounding organs. It also holds the heart in position and maintains a hollow space for the heart to expand into.

2.1 Structure of the heart wall

The heart wall consists of three layers; epicardium, myocardium, and endocardium (Figure 2.1). The epicardium is the outermost layer of the heart wall which is sometimes considered as a division of the inner layer of the pericardium. Epicardium is a thin layer with a

thickness of the order of 100 µm comprised mainly of connective tissue, which helps to lubricate and protect the heart. Below the epicardium is the second layer of the heart wall; myocardium.

The myocardium is the middle muscular layer of the heart wall which is composed of cardiac muscle cells (myocyte). Myocardium makes up the majority of the thickness and mass of the heart wall and is responsible for contraction and relaxation of the heart walls in order to pump blood. Below the myocardium is the thin endocardium.

The endocardium is the innermost layer of the heart wall, with an approximate thickness of 100 µm, which lines the inside of all four heart chambers and forms the surface of the valves. Endocardium is composed of connective tissue and a layer of endothelial cells which provide a smooth, non-adherent surface to keep the blood from sticking to the wall and forming blood clots.

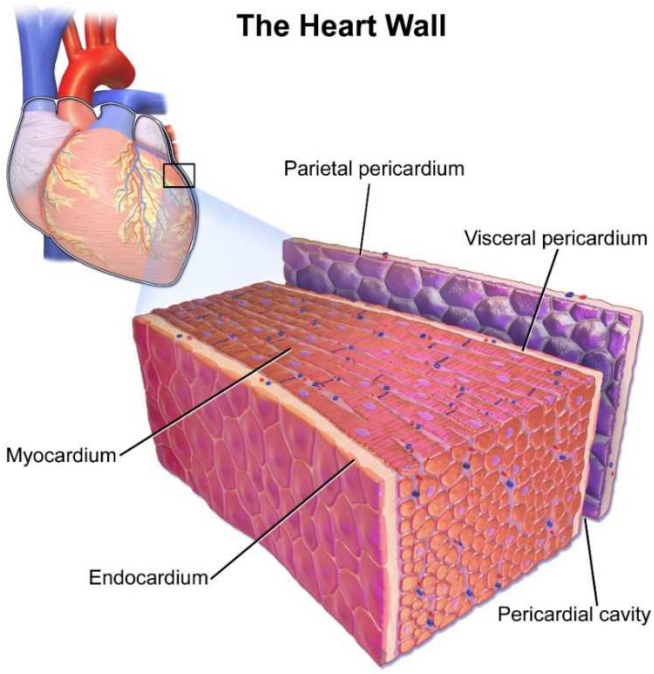

Figure 2.1: Heart wall consist of three layers; endocardium, myocardium and epicardium. Epicardium is sometimes considered a division of the visceral pericardium. (Source: wikipedia.org).

The wall thickness of the heart varies in different regions. The ventricles have thicker walls than the atria because they need to support higher pressures. In addition, the wall thickness

of the left heart is larger than that of the right heart due to the higher pressures in the left heart. The wall thickness also varies spatially within the ventricles; it is thickest at the base and thinnest at the apex.

2.2 Heart chambers

The heart contains four chambers; namely the right and left atria, and the right and left ventricles (Figure 2.2). The atria are smaller than the ventricles and have thinner walls. The atria are the blood receiving chambers of the heart and are connected to the veins that carry blood to the heart. The ventricles are the blood pumping chambers of the heart, and are connected to the arteries that carry the blood out of the heart to the body.

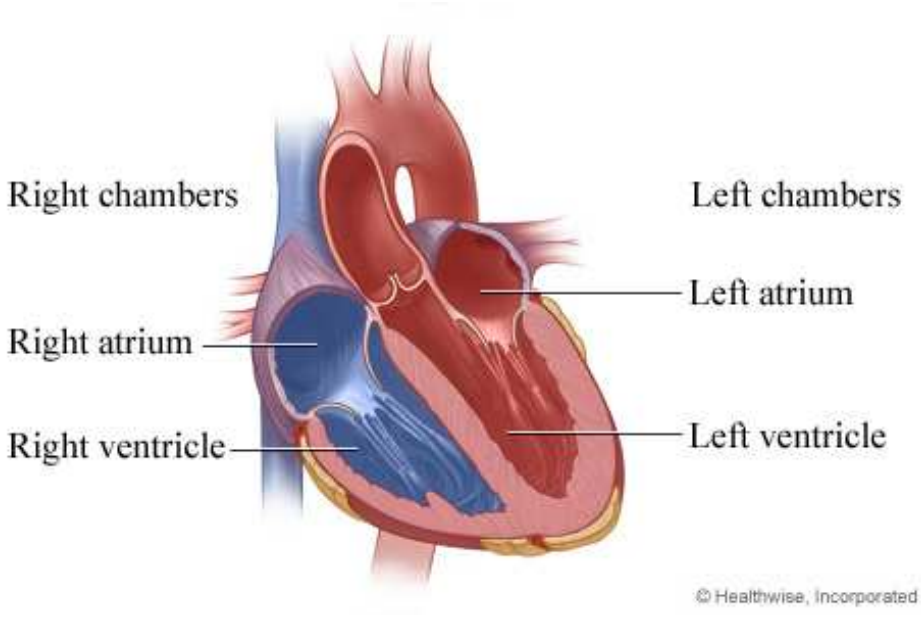

Figure 2.2: Chambers of the heart: right and left atria, and right and left ventricles.

The right atrium receives the deoxygenated blood from the body and pumps it to the right ventricle. The right ventricle pumps the deoxygenated blood to the lungs. The left atrium receives

the oxygenated blood from the lungs and pumps it to the left ventricle. And the left ventricle pumps the oxygenated blood to the entire body.

The left and right atrial appendages are ear-shape pouched that are connected to and drain into the left and right atria, respectively. In a normal heart the appendages contract rhythmically with the rest of the atria and squeeze the blood into the ventricles. It is unclear what function the appendages perform.

2.3 Heart valves

In order for a proper flow of the blood through the heart, and to prevent the blood from flowing backward (regurgitating) into the heart, a system of one-way valves are present in the heart (Figure 2.3). The valves control the flow of blood by opening and closing during the cardiac cycle. The opening and closing functions are controlled by the pressure differences through the heart, as well as some muscles in the heart. The heart valves can be broken down into two types: atrioventricular valves, and semilunar valves.

Atrioventricular valves (AV) are located between the atria and ventricles and only allow blood to flow from the atria to the ventricles and prevent blood regurgitation to the atria. The AV valve between the right atrium and right ventricle is called the tricuspid valve, because it has three leaflets (cusps), and the AV valve between the left atrium and left ventricle is called the mitral valve or bicuspid valve, because it has two leaflets.

Semilunar valves are located between the ventricles and major arteries and block the regurgitation of the blood back to the heart. The semilunar valve between the right ventricle and the pulmonary trunk that carries blood to the lungs is called pulmonary valve. And the semilunar valve between the left ventricle and the aorta is called the aortic valve.

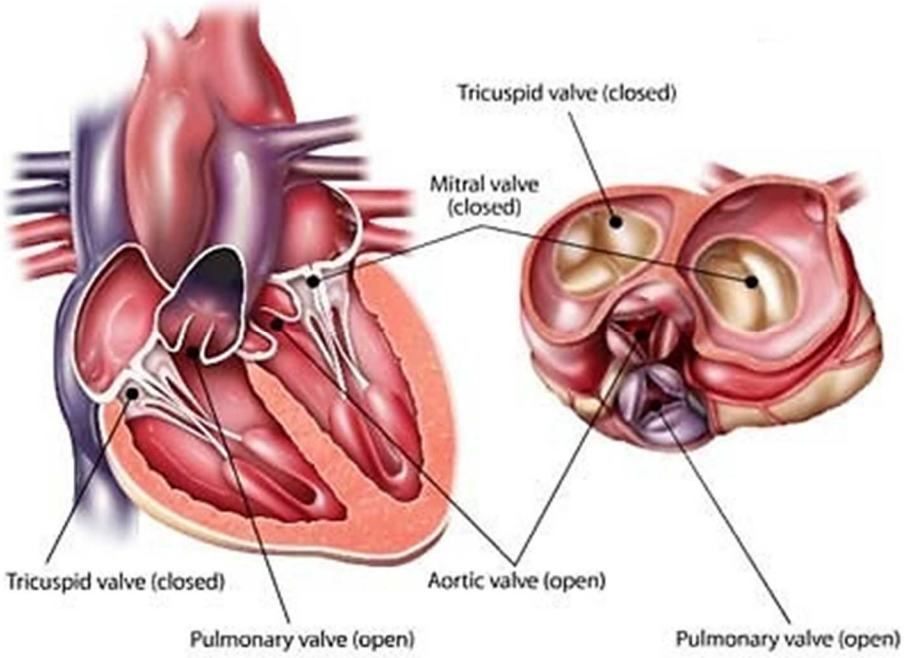

Figure 2.3: Anatomy of the heart valves. (Source: ksu.edu.sa).

The AV valves are connected to the ventricles via strong strings called chordae tendineae which keep them from folding backwards. The semilunar valves, on the other hand don't have chordae tendineae to keep the closed. Instead, their leaflets are cup-shape to catch the back flow and use the blood's pressure to shut.

2.4 Conduction system of the heart

The conduction system of the heart consists of myocytes and conducting fibers that initiate impulses and conduct them rapidly throughout the heart. The conducting system is able to initiate the cardiac cycle and coordinate the contractions of the heart chambers. In order for the heart to beat effectively, and for the pulmonary and systemic circulations to operate in synchrony the events in the cardiac cycle must be coordinated. The conduction system is made up of three

main components; the sinoatrial (SA) node located in the right atrium, the atrioventricular (AV) node located on the inter-atrial septum, and the His-Purkinje system located along the ventricular walls (Figure 2.3). Each heartbeat is initiated with an electrical potential generated in SA node. The signal spreads throughout the atria and depolarizes the atrial muscle which causes the myocytes to contract. The impulse then arrives at the AV node; where the impulse conduction is slowed down to allow sufficient time for atrial depolarization and contraction prior to ventricular depolarization. Then the impulse enters the base of ventricles through a pathway called the bundle of His, and then follows the left and right bundle branches through Purkinje fibers that conduct the impulses at a very high velocity. This results in rapid depolarization and contraction of myocytes throughout both ventricles.

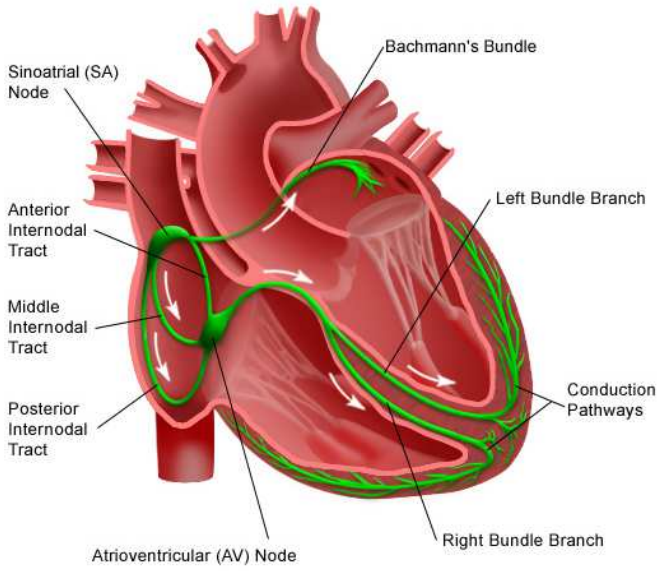

Figure 2.3: The conduction system of the heart. The electrical stimulus which is generated at SA node spreads throughout the atria via internodal tracts and Bachmann's bundle. The impulse then arrives at the AV node, travels through the bundle of His and follows the left and right bundle branches. (Source: choc.org)

2.5 Cardiac cycle

The cardiac cycle is the sequence of the events that occur in one heartbeat. One cardiac cycle can be divided into two phases; diastole and systole (Figure 2.4). Diastole is the period of time when the ventricles are relaxed. During most of this time period, blood is passively flowing from right and left atria into the right and left ventricles, respectively. The mitral valve and tricuspid valve are open during this time. The right atrium receives deoxygenated blood from the body through inferior vena cava (IVC) and superior vena cava (SVC). The left atrium receives oxygenated blood from the lungs through four pulmonary veins. At the end of diastole the atria contract which pushes an additional amount of blood into the ventricles.

Systole is when the right and left ventricles contract and pump the blood into the pulmonary trunk and the aorta, respectively. The mitral valve and tricuspid valve are closed during this time; therefore no blood is entering the ventricles. The pulmonary valve and aortic valve are open to allow the blood to eject into the pulmonary artery and aorta. During systole blood continues to enter the atria through vena cava and pulmonary arteries.

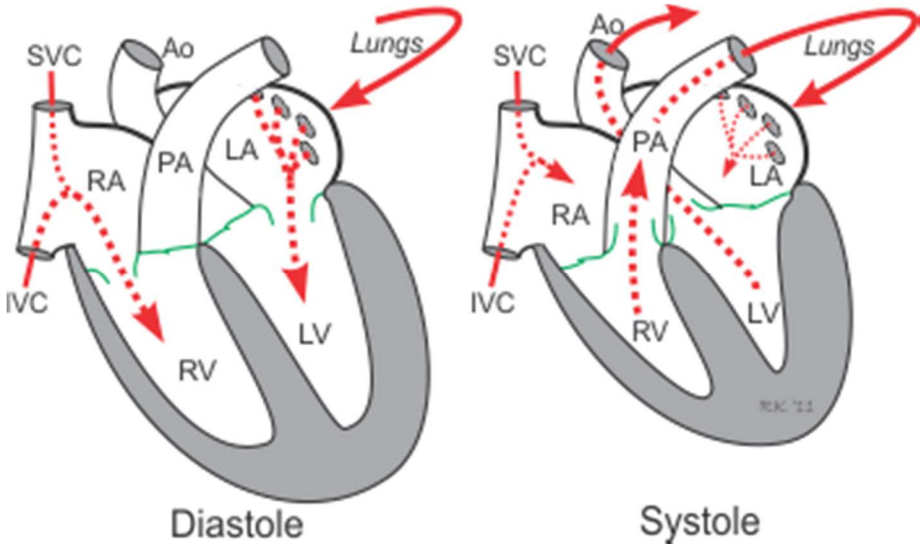

Figure 2.4: The cardiac cycle; blood flow in systole and diastole. (Source: cvphysiology.com)

2.6 Wigger's diagram

Wigger's diagram is a graph that shows the changes in the aortic pressure, left atrial pressure, left ventricular pressure, left ventricular volume, electrocardiogram (ECG), and heart sound during one cardiac cycle (Figure 2.5).

The first phase of the cardiac cycle is initiated by the P-wave of the ECG which corresponds to the atrial depolarization. As a consequence of the contraction of the atria, atrial pressure and ventricular volume increase. Atrial contraction normally accounts for 10% of ventricular filling in resting condition. At high heart rates when there is less time for passive filling this number may increase up to 40%. Passive and active filling of the ventricle also increases the ventricular pressure and volume. After the atrial contraction is complete, atrial pressure begins to fall which causes a reversal pressure gradient against the mitral and tricuspid valves, moving the valve leaflets upward. The ventricular volumes are maximal in this stage, which are called end diastolic volume (EDV).

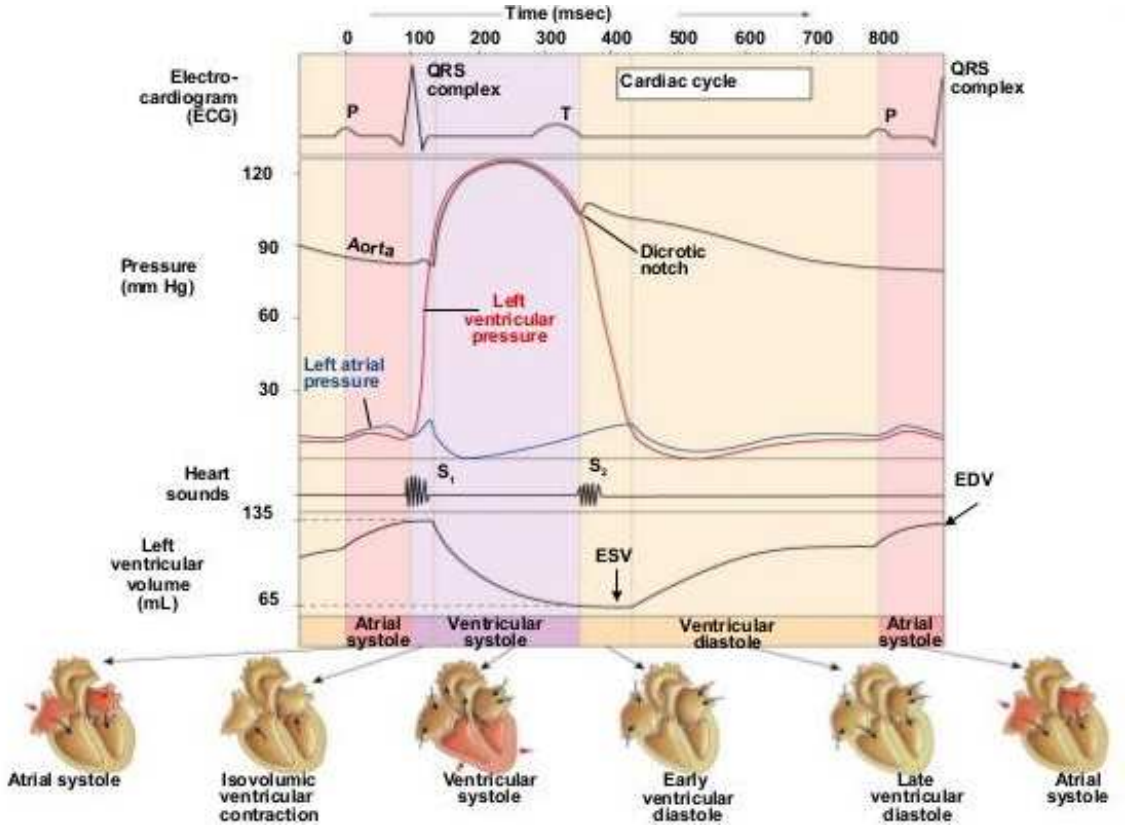

Figure 2.5: Wigger's diagram showing ECG, aortic pressure, left atrial pressure, left ventricular pressure, left ventricular volume, and heart sound (Benjamin Cummings, 2007).

The next phase is associated with the QRS complex of the ECG, which corresponds to the depolarization of the ventricular muscle. Ventricular contraction causes a rapid increase in ventricular pressure and the atrioventricular valves snap shut resulting in the first heart sound 'lub'. At this time all of the valves are closed, therefore ventricular volume does not change, i.e. there is no blood ejection. This is referred to as the isovolumetric contraction. Note that the volume of individual myocytes does change due to contraction and the ventricular geometry changes considerably.

As the ventricular pressure exceeds the pressure within the aorta and pulmonary artery, the semilunar valves open leading to rapid ejection of blood into aorta and pulmonary artery from the left and right ventricles, respectively. Ventricular volume decreases with blood leaving the

ventricles. Atrial pressure initially drops due to expansion of atrial chamber as the base of the atrium is pulled down. Blood continues to enter the atria from their inflow tracks and therefore the atrial pressure starts to increase.

T-wave corresponds to the repolarization of the ventricles which leads to a decrease in ventricular pressure. When the ventricular pressure drops sufficiently the semilunar valves snap shut causing the second heart sound 'dub'. The atrial pressure continues to rise since the blood is returning to the atria from the systemic and pulmonary circulations.

In the next phase, ventricles begin relaxing but the volume of the blood in the ventricles does not change because all of the valves are closed. This is referred to as the isovolumetric relaxation. The amount of blood that remains in the ventricles is called end systolic volume (ESV). The difference between the end diastolic volume and end systolic volume represents the stroke volume.

As the isovolumetric relaxation continues, at some point the ventricular pressure falls below the atrial pressure causing the atrioventricular valves to open and the ventricular filling begins. When the atrioventricular valves open, the atrial pressure drops rapidly. Although the ventricles are filling, since the relaxation still continues the ventricular pressure continues to slightly decrease. Once the relaxation is complete, the ventricular pressure starts to rise as the blood enters the ventricles. Aortic pressure gradually declines as the blood is entering the peripheral arteries.

2.7 Excitation- contraction coupling

Excitation-contraction coupling is a process where an electrical stimulus (action potential) triggers myocyte to contract. When a myocyte is depolarized (cells charge slightly positive) by an action potential, calcium ions enter the cell through L-type calcium channels

located on the sarcolemma triggering further release of calcium ions into the cytoplasm through calcium-release channels. This phenomenon is called calcium-induced calcium release. Calcium in the cytoplasm then binds to cardiac troponin-C, which is part of the regulatory complex attached to the thin filaments. When calcium binds to troponin-C it moves the troponin complex away from the actin binding site and frees the actin to be bound by ATP located on the myocin head. This binding provides the energy for a conformational changes in the actin myocin complex. This change results in a movement between actin and myocin heads where actin and myocin filaments slide past each other shortening the sarcomere length. Depolarization sustains as long as the calcium concentration remains elevated. At the end of this phase calcium entry into the cell slows and Intracellular calcium is removed by the sarcoplasmic reticulum, lowering intracellular calcium concentration and removing calcium form troponin-C returning it to its original position on the active site of actin. As the actin filaments return to their initial position contraction ends and the initial sarcomere length is restored (Figure 2.6).

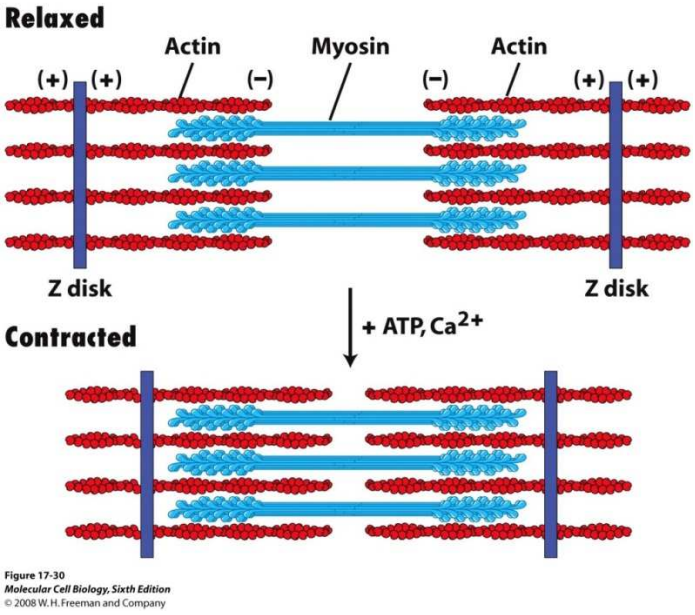

Figure 2.6: Contraction of the heart muscle occurs when the myosin thick filaments and actin thin filaments slide past each other, thus shortening the length of a sarcomere. Muscle fiber in the relaxed (above) and contracted (below) positions. Source (miami.edu)

CHAPTER 3: MECHANICS OF MYOCARDIUM

3.1 Myocardial Morphology and Structure

Myocardial muscle (cardiac muscle) is one of the three major types of muscle, the other two being skeletal muscle, and smooth muscle. Myocardial muscle is a striated muscle composed of tubular muscles called myocytes, which are in turn composed of many chains of myofibrils (Figure 3.1). Myofibrils are composed of repeating functional units called sarcomeres. Sarcomeres are the smallest contractile elements of myofibril and are composed of thick myosin filaments and thin actin filaments that slide past each other when the muscle contracts or relaxes.

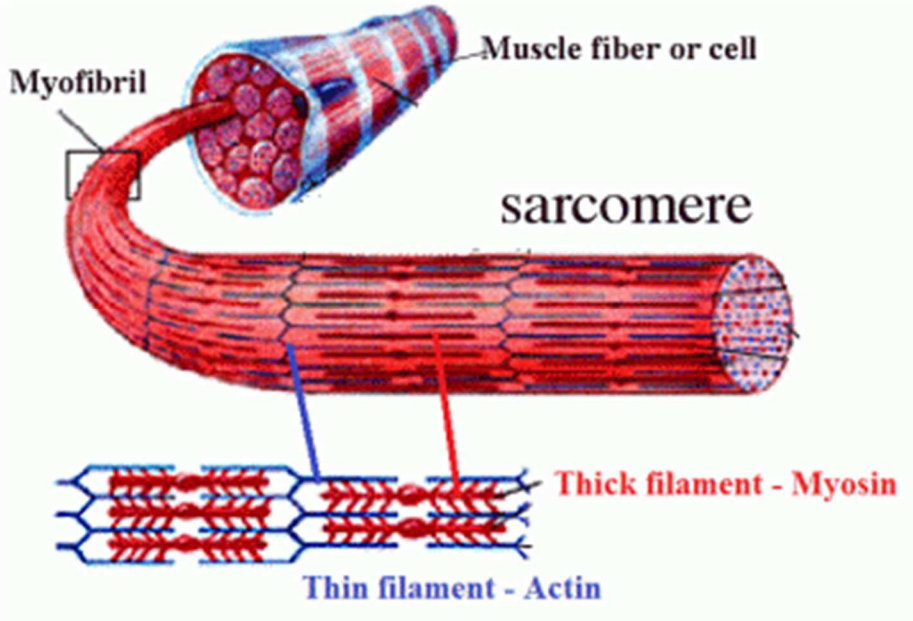

Figure 3.1: Microstructure of the myocardium. (Source: wordpress.com)

Ventricular myocytes are arranged in discrete bundles or layers separated by cleavage planes. The layers are three to four cells thick and there is some branching between the adjacent layers. Because of the approximately-parallel alignment of the adjacent myocytes, a mean myocyte axis vector can be defined at any point which is referred to as the mean fiber orientation. Fiber orientation changes continuously through the myocardial wall thickness. Figure 3.2-a depicts the 3D layered organization of myocytes from epicardium to endocardium. Figure 3.2-c illustrates the fiber orientation of five different circumferential-longitudinal sections at different transmural depths of the left ventricle wall. Studies on the architecture of the left ventricle suggest that in the equatorial region, the fiber angle with respect to circumferential direction changes from +50° to +70° in the sub-endocardial region to 0° in the mid-wall region to -50° to -70° in the sub-epicardil region[9]. Figure 3.2-d is a schematic of the 3D organization of myocytes. Myocytes are connected to adjacent myocytes by a regular array of radial collagen fibers. Also, a network of connective tissue surrounds the myocytes and the adjacent myocyte layers are loosely coupled by sparse and relatively long collagen fibers.

At any point within the myocardium, three distinct material axes can be identified; one is the fiber axis which coincides with the fiber orientation, the second is the sheet axis which is transverse to the fiber axis in the plane of myocyte layer, and the third is normal axis which is perpendicular to that plane. Figure 3.2-e demonstrates a cube of the tissue with its local material coordinates.

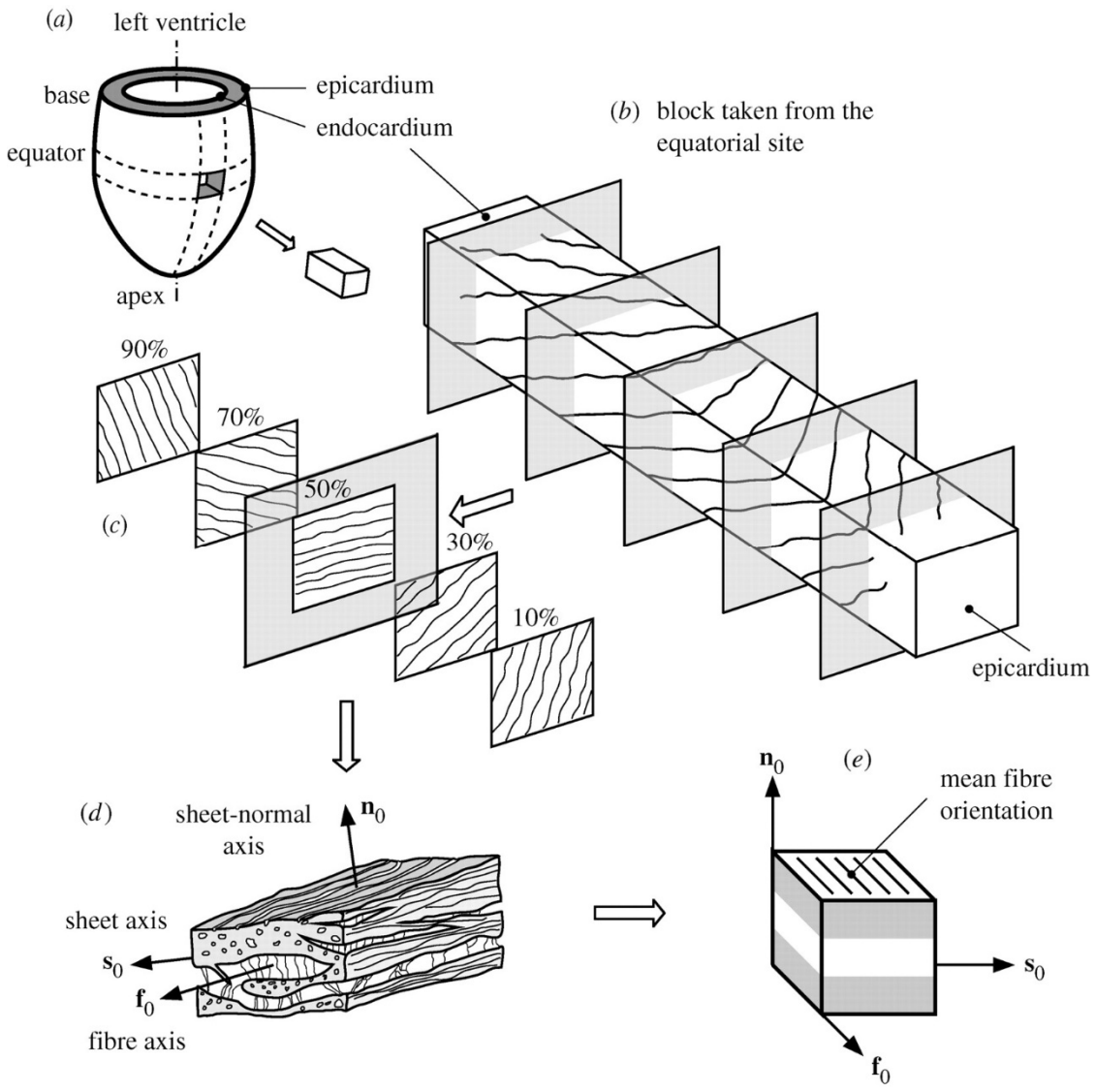

Figure 3.2: (a) Schematic of the left ventricle and a block cut from the eqator; (b) transmural variation of the fiber orientation from epicardium to endocardium; (c) transmural varioation of the fiber orientation on five longitudinal-circomferential sections at regular intervals of the wall thickness; (d) a layered organization of myocytes and and the collagen fibers between the layers, and the material coordinate system with fiber axis f_o, sheet axis s_o, and sheet-normal axis n_o; (e) a cube of the layered tissue with local material coordinates[9].

3.2 Mechanical behavior of the passive tissue

A heart muscle in the resting state is a non-homogeneous, orthotropic, and incompressible material. Heart muscle in the resting state exhibits the characteristics of viscoelastic materials; including stress relaxation under maintained stretch, creep under

maintained stress, and hysteresis in cyclic loading. However, since the relaxation time of the viscoelastic response is longer than the cardiac cycle, viscoelasticity is not important in mechanical modeling of the material on the time scale of the cardiac cycle.

A constitutive model or constitutive equation is a mathematical model that describes the physical properties of a given material. Many of the materials around us can be described by one of the three idealized, simplified stress-strain relationships, namely, the Newtonian viscous fluid, the non-viscous fluid, or the Hookean elastic solid. However, most biological materials including soft tissue do not fall under any of these categories. For this type of material physical laws are not sufficient to describe the material response; therefore, additional equations need to be established in the form of constitutive laws that can approximate the observed physical behavior of the material under specific condition.

Constitutive equations enable us to specify the stress components in terms of other field variables such as strain and temperature and are specific to a material or substance. There are two approaches in formulating the constitutive equations of soft tissue; phenomenological and structural. Phenomenological equations describe the macroscopic nature of the material and are mainly concerned with fitting a mathematical model to the experimental data. These models are not capable of relating the mechanism of deformation to the microscopic structure of the tissue. Unlike phenomenological relations, Structural constitutive relations are formulated by taking into account the microscopic structure of the material. Consequently, the parameters embodied in these equations are directly related to the tissue's morphology and structure.

The constitutive equation of an isothermal elastic body may be expressed in the general form

$$\sigma = g(F)$$

(3.1)

where g is referred to as the response function associated with the Cauchy stress tensor σ.

A hyperelastic material, which is a subclass of elastic material, postulates the existence of a Helmholtz free-energy function Ψ which is defined per unit reference volume. In the case where $\Psi = \Psi(F)$ is only a function of some strain tensor F, the Helmholtz free-energy function is called strain energy function. Strain energy function is a scalar-valued function of a tensor variable. The response functions of a hyperelastic material $\hat{G}$ an g have physical expression of the form

$$P = \hat{G}(\mathrm{F}) = \frac{\partial \Psi(F)}{\partial F}$$

(3.2)

where P is the first Piola-Kirchhoff stress tensor. And by use of relation

$$\sigma = J^{-1} P F^T$$

where σ is the Cauchy stress tensor, and $J = \det F$ is the Jacobian of the deformation tensor F, we have

$$\sigma = g(F) = J^{-1} \frac{\partial \Psi(F)}{\partial F} F^T$$

(3.3)

3.2.1 Generalized Fung hyperelastic constitutive model

The generalized Fung's strain energy function has the following form:

$$\mathrm{W} = \frac{c}{2}(e^Q - 1) + \frac{1}{D}\left(\frac{J_{el}^2 - 1}{2} - \ln J_{el}\right)$$

(3.4)

where W is the strain energy per unit reference volume, c and D are the temperature-dependent material parameters, J_{el} is the elastic volume ratio, and Q is defined as:

$$Q = E:(bE) = b_{ijkl}E_{ij}E_{kl}$$

(3.5)

where b is a dimensionless symmetric forth-order tensor of anisotropic material constants, and E is the Green-Lagrange strain tensor. The number of independent components of b is 21 for anisotropic, and 9 for orthotropic materials.

Under the assumption of tissue incompressibility, $J_{el} = 1$, the Fung strain energy equation is reduced to :

$$\mathrm{W} = \frac{c}{2}(e^{Q} - 1)$$

(3.6)

For a planar biaxial testing, the out of plane normal and shear stresses are considered zero. Therefore, the full expansion of the quadratic terms of Q including the in-plane shear strains has the following form

$$Q = b_{1111}E_{11}^2 + b_{2222}E_{22}^2 + 2b_{1122}E_{11}E_{22} + b_{1212}E_{12}^2 + 2b_{1112}E_{12}E_{11} + 2b_{2212}E_{12}E_{22} \quad (3.7)$$

In practice, the shear strains in the biaxial testing is nearly zero, so the shear terms of Q can be eliminated and equation (3.7) can be written as:

$$Q = b_{11}E_{11}^2 + b_{22}E_{22}^2 + 2b_{12}E_{11}E_{22}$$

(3.8)

To date, this is perhaps the most broadly used constitutive model for the biaxial response of soft tissues.

CHAPTER 4: MATERIALS AND METHODS

4.1 Specimen preparation

Fresh healthy sheep hearts (n=21) were obtained from a local abattoir on the morning of harvest. Left and right ventricles were cut open and thin planar slices were obtained from the middle layer of ventricular free wall using a commercial meat slicer (Figure 4.1).

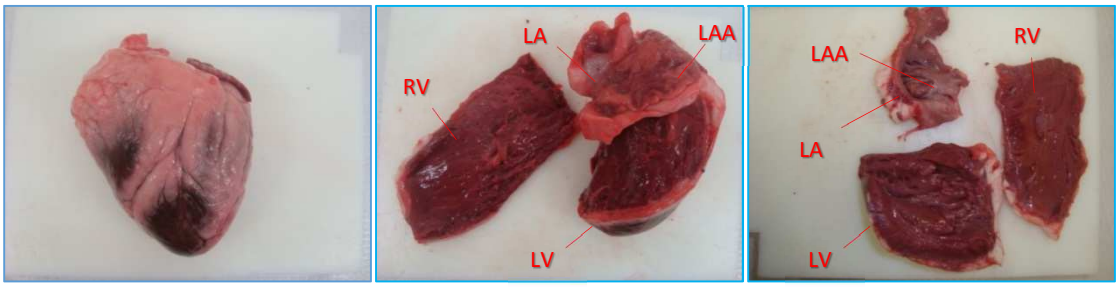

Figure 4.1: Fresh sheep hearts were obtained from a local abattoir. Right and left ventricles and atria were cut open. Ventricl were then held flat against the blade of a meat slicer and thin planar slices were obtained.

Square specimens were excised from anterior and posterior portions of the left and right ventricular free wall (Figure 4.2 and Figure 4.3). Samples were cut in such a way that the edges were parallel and perpendicular to predominant fiber direction as judged by eye. In addition, left and right atria were cut open and square samples were excised from anterior and posterior portions of the full thickness atrial free wall. Specimens were oriented in such a way that two of the edges were parallel to the main fiber directions. As such, in most samples one pair of edges was maintained parallel to the midplane of the atrioventricular valves. Additionally, two samples were excised from left and right atrial appendages. Samples were cut with two edges parallel to

the most prominent direction of the pectinate muscles visible on the internal surface. Samples thickness and length were measured at several locations using Mitutoyo Digital caliper (Model 500-754-10). Following the measurements, the specimens were stored in phosphate buffered saline (PBS) solution at room temperature. All mechanical testing was completed within 6 hours after heart harvest (n = 19 used for mechanical testing and remaining n = 2 used for histological analysis).

Figure 4.2: Square sample were excised form different anatomical regions of the sheep heart and strored in PBS solution.

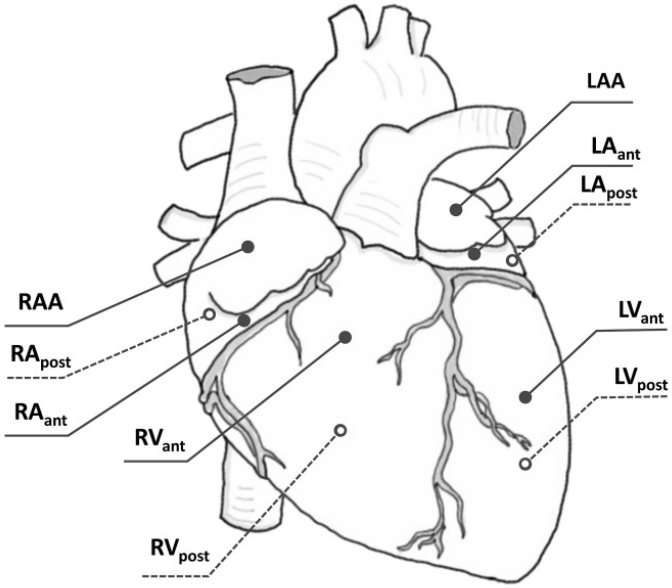

Figure 4.3: Approximate location of tissue specimens cut from the anterior and posterior portion of the left and right ventricles (LV and RV), left and right atria (LA and RA), and left and right atrial appendages (LAA and RA

4.2 Biaxial testing system

A planar biaxial stretching system (CellScale, Waterloo, Canada) was used to determine mechanical properties of the heart specimens (Figure 4.4). Details of the biaxial testing procedure have been previously described[1]. Briefly, tissue specimens were mounted onto the test apparatus using a set of four CellScale BioRakes oriented along two mutually perpendicular axes. Specimens were positioned such that the fiber and cross-fiber directions were aligned parallel to x and y axes, respectively. The biaxial system equipped with two 1000g load cells located on the two orthogonal arms (Model 31, Honeywell Inc., Columbus, OH). Specimens were immersed into a temperature-controlled normal saline bath heated to 37°C to simulate the physiological environment. Prior to initiation of loading, the load cells were zeroed. The top sides of tissue samples were sprinkled with graphite powder to enable tracking of tissue deformation. Real-time displacement of the graphite markers was obtained at a rate of 15Hz using a camera placed over the top surface. Tissue specimens were subjected to equibiaxial displacement-controlled loading in the form of true strain. Specimens were preconditioned by 10 cycles of 10% equibiaxial strain at 0.5Hz. Subsequently, each specimen underwent an equibiaxial strain of up to 50% (40% for the ventricles and 50% for the atria and atrial appendages) with a 4s stretch and a 4s recovery duration. Following the mechanical testing, CellScale LabJoy image tracking was used to capture displacement field. Relative movements of the center-element nodes were used to calculate deformation gradient and green strain tensor in MATLAB (v8.1.0.604, Natick, MA).

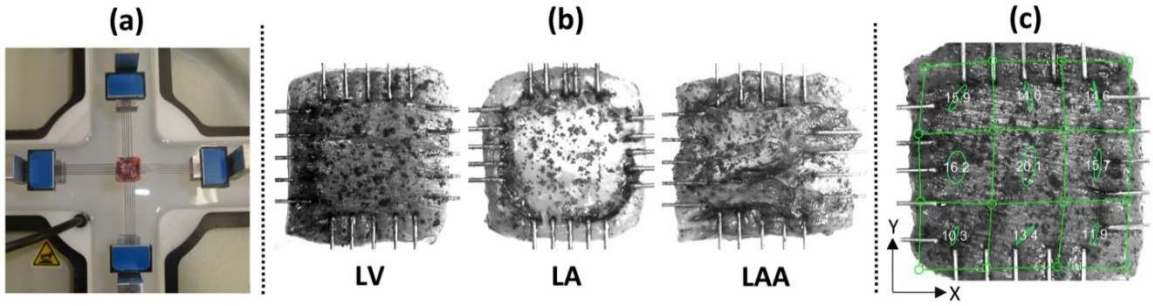

Figure 4.4: CellScale planar biaxial stretching apparatus (a), representative specimens from different heart chambers (b), and CellScale LabJoy image tracking software was used to obtain strain maps (c).

4.3 Constitutive modeling

Since soft tissues are mainly comprised of water, our samples were assumed to be nearly incompressible. Planar forces (F_{11}, F_{22}) measured by the two load cells were used to calculate Cauchy stresses (T_{11}, T_{22}) in the fiber and cross-fiber directions, respectively.

$$T_{11} = \lambda_1 \frac{F_{11}}{t_0 l_0} \quad \text{and} \quad T_{22} = \lambda_2 \frac{F_{22}}{t_0 l_0}$$

(4.1)

where t_0 is tissue thickness in the initial condition, and $\lambda = l/l_0$ is stretch ratio representing the ratio of deformed tissue length (l) to resting length (l_0). Components of Green strain tensor (E) were calculated using the following equations:

$$E_{11} = \frac{1}{2}(\lambda_1^2 - 1) \quad \text{and} \quad E_{22} = \frac{1}{2}(\lambda_2^2 - 1)$$

(4.2)

A four parameter Fung exponential strain energy function[5] was fitted to the stress-strain data

$$W = \frac{C}{2}(e^Q - 1), \quad Q = c_{11}E_{11}^2 + 2c_{12}E_{11}E_{22} + c_{22}E_{22}^2$$

(4.3)

where E_{11} and E_{22} are the Green strains in x and y directions, respectively. Furthermore, c_{11}, c_{22}, c_{12}, *and* C are the material constants. Cauchy stresses can be obtained based on the following equations:

$$T_{11} = \lambda_1^2(c_{11}E_{11} + c_{12}E_{22})C\ exp(Q) \text{ and}$$

$$T_{22} = \lambda_2^2(c_{12}E_{11} + c_{22}E_{22})C\ exp(Q)$$

(4.4)

A Levenberg-Marquardt least squares algorithm in MATLAB (v8.1.0.604) was used to fit the Fung strain energy function to the experimental data.

Although arm displacement rates were set equal for both circumferential and longitudinal directions, strain applied to the center of the specimen was not exactly equal in the two directions, due to initiation and propagation of tears in the tissue at the boundaries where tungsten wires are anchored (Figure 4.4). Therefore, stress-strain relationships in the equibiaxial strain state ($E_{11} = E_{22} = E$) were obtained as:

$$T_{11}^{equi} = (2E + 1)E(c_{11} + c_{12})Cexp\{(c_{11} + c_{22} + 2c_{12})E^2\} \text{ and}$$

$$T_{22}^{equi} = (2E + 1)E(c_{12} + c_{22})Cexp\{(c_{11} + c_{22} + 2c_{12})E^2\}$$

(4.5)

where the superscript *equi* denoted equibiaxial condition. The stress-strain curves converted to the equibiaxial stretch condition were used to determine the degree of tissue anisotropy. Tissue anisotropy was evaluated by the difference in material coefficients between the two directions as:

$$K = \frac{2|c_{11} - c_{22}|}{(c_{11} + c_{22} + 2c_{12})}$$

(4.6)

In addition, Equation 4.3 was used to calculate the strain energy stored in the specimens at equibiaxial strains of $E_{11} = E_{22} = 0.10$, 0.15, and 0.20. The strain levels were chosen to embrace a wide range of deformation observed in *in vivo* strain measurements[12].

4.5 Data averaging

Curve averaging as opposed to coefficient averaging is the appropriate approach to summarize the nonlinear material properties of biomedical materials[23]. Therefore to obtain average curves of each specimen, Cauchy stresses were obtained at equally spaced intervals of strain using Equation 4.5. At each strain increment Cauchy stress values were then averaged to obtain a single data set for each anatomical region. The strain ranged from 0 to 0.5 for the atria, 0 to 0.4 for the atrial appendages, and from 0 to 0.2 for the ventricles. Although ventricles were subjected to 40% strain, in most of the samples tears were initiated at the edge of boundaries at lower stretch levels, so we were not able to stretch further. Therefore, for all of the regions the average curves were only extended to a strain level where actual experimental data were available for more than 80% of the samples. Samples which failed to stretch to that strain level were excluded from the average. The averaged data were then fitted to the Fung constitutive model to determine a single set of material coefficients for each region.

4.6 Statistical analysis

All statistical analyses were performed in SPSS 16.0. All values are reported as mean ± standard deviation (SD), and a p value less than 0.05 was regarded as statistically significant. Shapiro-Wilk test of normality with an alpha level of 0.05 was performed to ensure normal distribution of the strain energy data. Paired-samples t-test was used where comparing the strain energy values between two locations, and one-way ANOVA followed by a Games Howell post

hoc test was used to compare strain energy values among three locations. To complement statistical analysis, Cohen's d effect size was reported as a measure of strength of relationship between the variables.

4.7 Histology

Tissue specimens from different anatomical regions were analyzed in terms of fiber structure and content using histology. Fresh specimens were extracted from left and right ventricles, atria, and atrial appendages as described previously. Atrial specimens were investigated at two different transmural depths, one section was taken from the internal collagenous membrane, and another section was taken deeper into the tissue. Ventricular specimens were excised from mid wall. All the samples were imbedded in paraffin and sectioned at a thickness of 4 microns on a microtome. Sections were cut parallel to the endocardial layer. After being put into an oven (~ 60 degree C) and cooled, the slides were stained with Masson's trichrome stain (Figure 4.5). The Masson's trichrome stain rendered myocytes red and collagen fibers blue. A custom MATLAB code was developed to determine the surface area ratio of collagen to myocyte via image thresholding based on RGB (red, green, and blue) values.

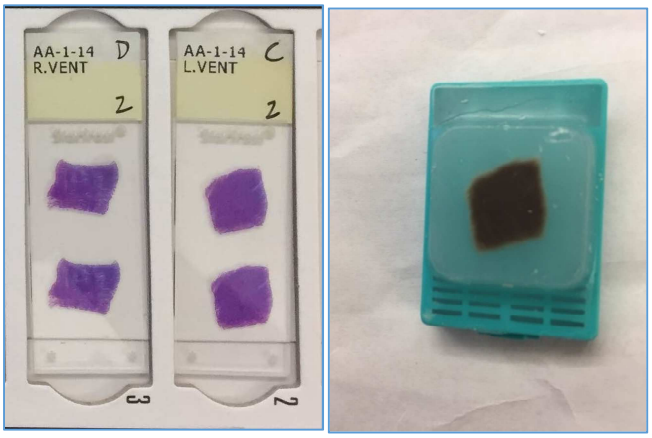

Figure 4.5: Histology analysis; the paraffin embedded tissue sample on the right, and Masson's trichrome stained sections on the left.

CHAPTER 5: RESULTS

A total of 189 square specimens were excised to determine passive mechanical properties of healthy ovine heart chambers (18 specimens from LAA and 19 specimens from each of the other regions). Average length and thickness of the samples are presented in Table 5-1. Mechanical properties of the samples were determined by the planar biaxial stretching system. Experimental raw data of the tissue specimens from the left side of the heart are shown as Cauchy stress–Green strain plots in the fiber and cross-fiber directions in Figure 5.1. In addition, stress–strain response of the tissue specimens from the right heart chambers is presented in Figure 5.2. The variations in the mechanical properties of the samples from the same location of the heart are due to the natural inter-subject differences. All regions demonstrated nonlinear response to strain during the testing protocol both in fiber and cross-fiber directions. However, nonlinearity of left and right atria and atrial appendages was more pronounced than the ventricles. Furthermore, stress-strain curves of the left and right ventricles had a greater slope in the main fiber direction than the cross-fiber direction, i.e. the tissue was significantly stiffer in the fiber direction than the cross fiber direction. This trend was not pronounced in the atria and atrial appendages. The ventricles had the greatest slope of the stress-strain curves among all regions, followed by the atrial appendages and lastly by the atria.

Table 5-1: Dimensions of the specimens in stress-free condition

	LV_{ant}	LV_{post}	LA_{ant}	LA_{post}	LAA	RV_{ant}	RV_{post}	RA_{ant}	RA_{post}	RAA
Length (mm)	11.5±0.9	11.1±0.9	9.6±1.2	10.5±1.5	11.1±1.1	11.2±1.2	11.1±1.0	9.9±1.3	9.9±1.0	11.0 ±0.9
Thickness (mm)	2.0±0.5	2.2 ± 0.2	2.1±0.3	2.2 ± 0.5	2.1± 0.5	2.0±0.3	2.1± 0.3	1.9±0.3	1.8±0.3	2.6± 0.4

Fung strain energy function was used to fit the Cauchy stress-Green strain data for each individual sample and material coefficients were obtained. The average ratio of shear stress to normal stress in the fiber direction at a strain level of 0.13 was found to be 3.3 ± 2.8% for LV, 1.4 ± 1.4% for LA, 3.9 ± 3.1% for LAA, 3.1 ± 1.7% for RV, 2.3 ± 2.3% for RA, and 3.1 ± 2.8% for RAA. Therefore, in this study, shear stresses were considered to be negligible compared to normal stresses in the biaxial experiments. Individual coefficient set of each tissue specimen is reported in the Appendix 1. The root mean square (RMS) values of curve fitting were low and averaged 1.84 ± 1.52 KPa showing an excellent fit of the model to the raw data. The material coefficients were then used to calculate the anisotropy index (Equation 4.6). Table 5-2 presents the average index of tissue anisotropy for all the anatomical regions. Paired sample t-test between anterior and posterior portions of ventricles and atria showed no significant difference in tissue anisotropy ($p>0.16$). Furthermore, statistical analysis revealed that the ventricles had higher anisotropy than other regions ($p<0.01$). Tissue anisotropy in the left ventricle was significantly higher than the right ventricle ($p<0.001$). However, the difference between left and right atria, and left and right appendages was not statistically significant ($p=0.24$ and $p=0.93$, respectively). Furthermore, the index of anisotropy of the left atrium was not significantly different than that of the left atrial appendages ($p=0.43$); however, the right atrium was significantly higher than the right atrial appendage ($p<0.01$).

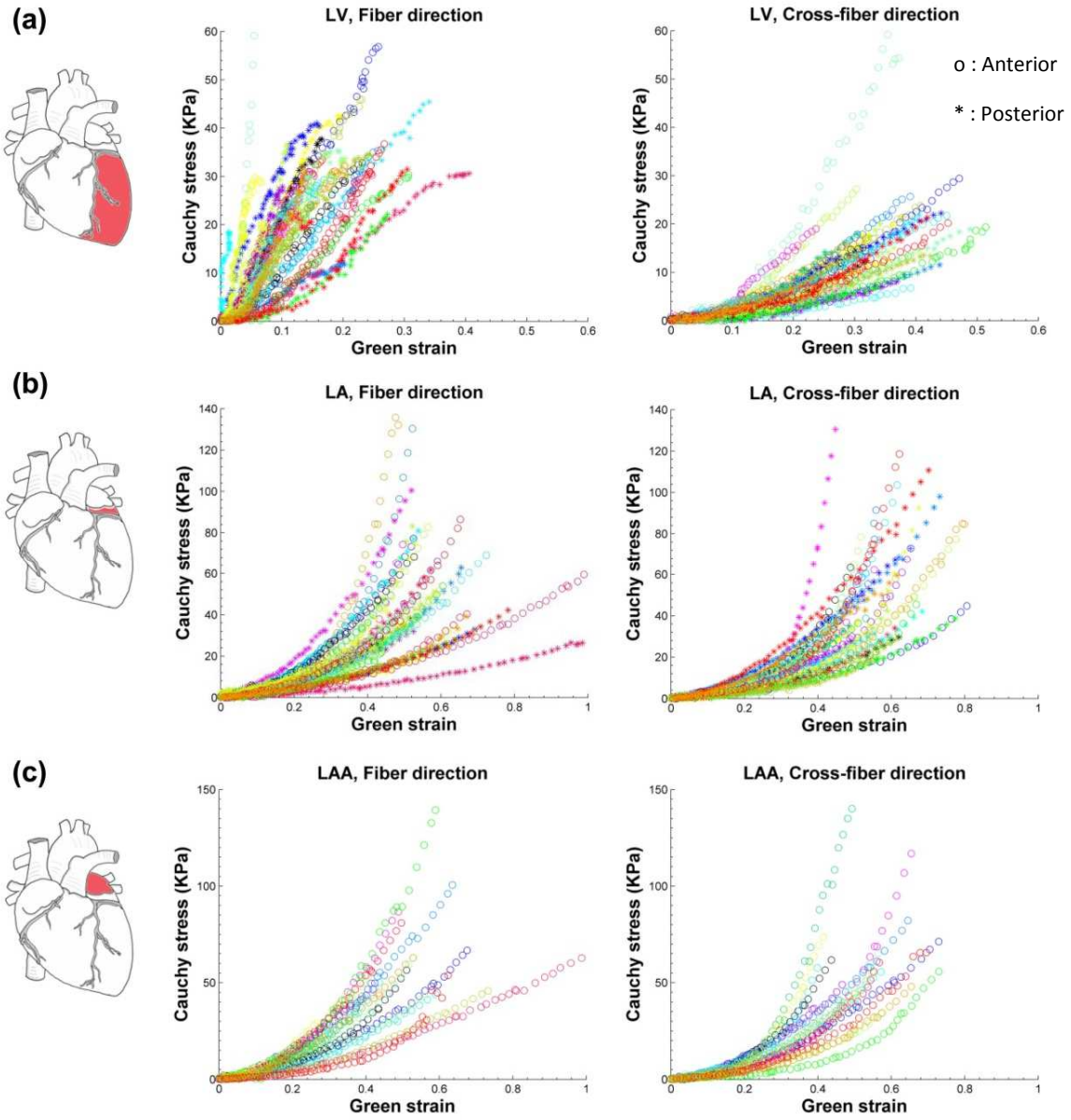

Figure 5.1: Cauchy stress-Green strain data for tissue specimens obtained from the left heart chambers in the fiber and cross fiber directions: (a) left ventricle, (b) left atrium, and (c) left atrial appendage (anterior regions: circle, and posterior regions: asterisk).

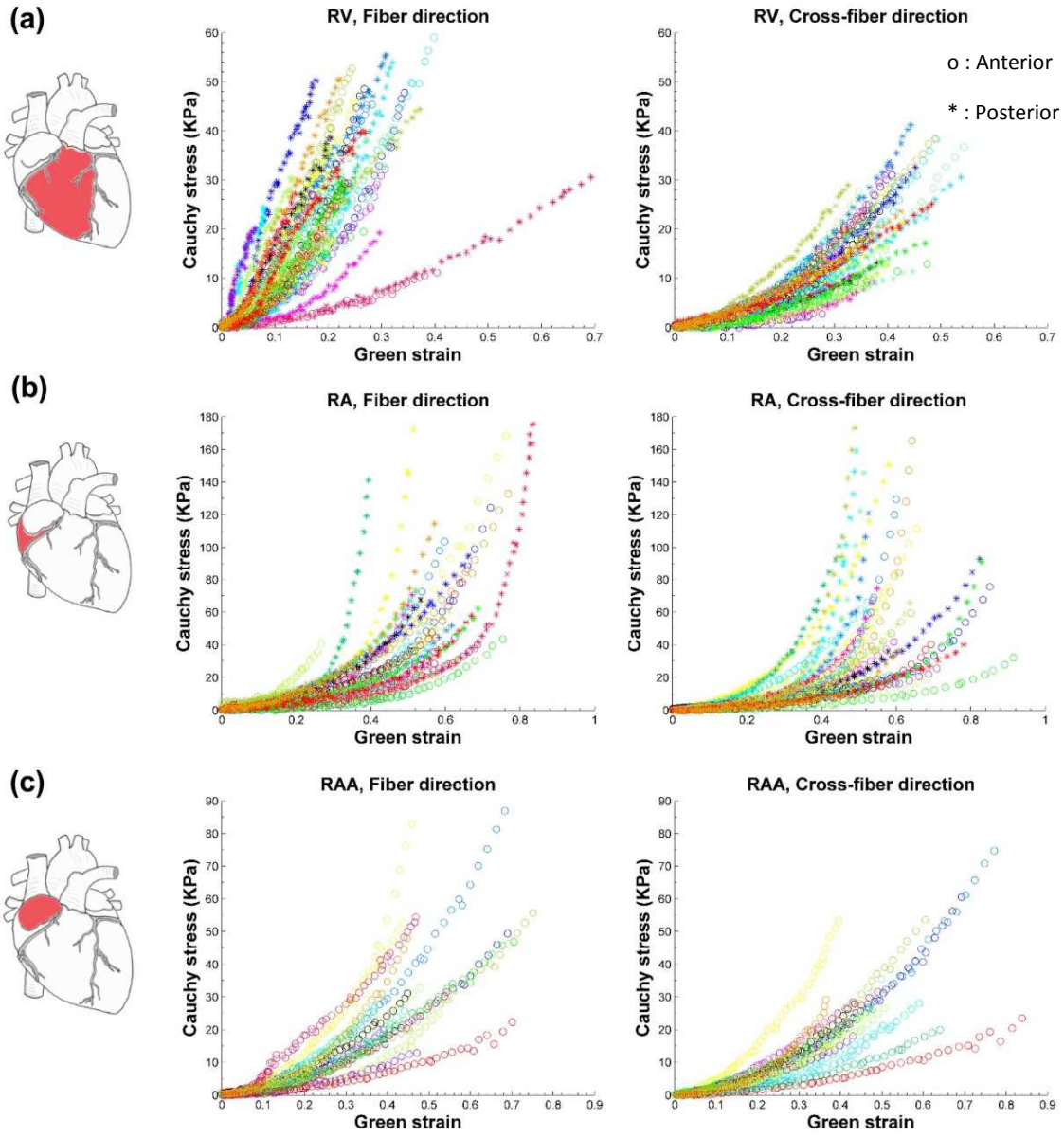

Figure 5.2: Cauchy stress-Green strain data for tissue specimens obtained from the right heart in the fiber and cross fiber directions: (a) right ventricle, (b) right atrium, and (c) right atrial appendage (anterior regions: circle, and posterior regions: asterisk).

Table 5-2: Index of tissue anisotropy for different anatomical regions

	LV_{ant}	LV_{post}	LA_{ant}	LA_{post}	LAA	RV_{ant}	RV_{post}	RA_{ant}	RA_{post}	RAA
Tissue anisotropy index (K)	1.1±0.5	1.1±0.5	0.3±0.3	0.4±0.3	0.3±0.2	0.7±0.4	0.9±0.4	0.5±0.3	0.4±0.3	0.3±0.2

The different anatomical regions of the heart were also compared based on the magnitude of strain energy function. Strain energy is the energy stored in the specimen undergoing a particular amount of deformation. Thus, strain energy can be used as an indicator of tissue stiffness. Strain energy was calculated for all the specimens at equibiaxial strains of $E_{11} = E_{22} =$ 0.10, 0.15, and 0.20. The mean value and standard deviation of strain energy for each anatomical region are presented in Table 5-3. The strain levels were chosen to embrace a wide range of deformation observed in in-vivo strain measurements. Magnitude of circumferential and longitudinal strains in normal healthy hearts is in the range of 0.10 to 0.20 in the end of systole and diastole[12]. Comparisons were made between the different anatomical regions in three steps as described below. First, the anterior and posterior portions of all heart chambers, namely left and right ventricles and left and right atria were compared together. Next, the right side of the heart was compared to the left side of the heart, meaning that each chamber from the right side was compared to the corresponding chamber from the left side. Lastly, the three anatomical regions on each side of the heart, namely ventricle, atrium and the atrial appendage were compared.

Table 5-3: Mean ± SD of the strain energy for different anatomical regions at 0.10, 0.15, and 0.20 strain levels

Region	$W_{10\%}$ (KPa)	$W_{15\%}$ (KPa)	$W_{20\%}$ (KPa)
LV_{ant}	0.7741 ± 0.2784	1.8107 ± 0.6705	3.4342 ± 1.4381
LV_{post}	0.7065 ± 0.2744	1.6756 ± 0.6790	3.2470 ± 1.5029
LA_{ant}	0.2291 ± 0.0733	0.5234 ± 0.1665	0.9510 ± 0.2999
LA_{post}	0.2474 ± 0.0703	0.5618 ± 0.1612	1.0118 ± 0.2952
LAA	0.3246 ± 0.0886	0.7410 ± 0.2020	1.3448 ± 0.3676
RV_{ant}	0.4508 ± 0.1423	1.0362 ± 0.3163	1.9004 ± 0.5553
RV_{post}	0.6089 ± 0.2393	1.3855 ± 0.5320	2.5036 ± 0.9300
RA_{ant}	0.1540 ± 0.0560	0.3525 ± 0.1286	0.6418 ± 0.2363
RA_{post}	0.1619 ± 0.0699	0.3748 ± 0.1624	0.6946 ± 0.3040
RAA	0.2209 ± 0.0948	0.5037 ± 0.2152	0.9123 ± 0.3877

The results of paired sample t-test between anterior and posterior portions of the ventricular and atrial chambers are listed in Table 5-4. Statistical analysis revealed no statistically significant difference in strain energy storage between anterior and posterior portions of the left atrium ($0.365<p<0.467$), and anterior and posterior portions of the right atrium ($0.472<p<0.638$) at all the three strain levels. Similarly, no statistically significant difference was observed between anterior and posterior portions of the left ventricle ($0.273<p<0.606$). However, strain energy stored by posterior specimens of the right ventricle were found to be statistically significantly greater than that stored by anterior specimens ($0.009<p<0.010$). In addition, Table 5-4 displays the Cohen's d effect size and the probability of superiority. Looking at the comparison between anterior and posterior portions of the right ventricle at strain of 0.15, there is a 71.42% chance that a sample picked at random from the posterior portion will have a higher strain energy value than a sample picked at random from the posterior portion.

Table 5-4: Comparison of the strain energy at 0.10, 0.15, and 0.20 strain levels between the anterior and posterior regions of the ventricular and atrial chambers

Region	$W_{10\%}$				$W_{15\%}$				$W_{20\%}$			
	t	p	Cohen's d	Probability of superiority %	t	p	Cohen's d	Probability of superiority %	t	p	Cohen's d	Probability of superiority %
LV_{ant} vs. LV_{post}	1.130	0.273	0.24	55.62	0.870	0.396	0.20	55.62	0.524	0.606	0.13	52.82
RV_{ant} vs. RV_{post}	2.627	0.009	0.80	71.42	2.607	0.009	0.80	71.42	2.566	0.010	0.79	71.42
LA_{ant} vs. LA_{post}	0.930	0.365	0.25	58.4	0.852	0.405	0.23	55.62	0.743	0.467	0.20	55.62
RA_{ant} vs. RA_{post}	0.479	0.638	0.12	52.82	0.586	0.565	0.15	55.62	0.734	0.472	0.19	55.62

The results of paired sample t-test between the right and the left heart chambers are tabulated in Table 5-5. For this analysis anterior and posterior portions of each region were pooled together to provide one representative data set for the region. Based on the statistical analysis, strain energy storage in left ventricle was significantly higher than the right ventricle at all the three strain levels ($1.35E\text{-}4<p<4.56E\text{-}4$). Likewise, the left atrium was found to be

significantly stiffer than the right atrium (1.16E-6<p<4.20E-6). Furthermore, strain energy values of left atrial appendage were significantly greater than those of right atrial appendage (p=0.002). In brief, all chambers from the left side of the heart have significantly higher strain energy than the corresponding chambers on the right side of the heart at all the three strain levels.

Table 5-5: Comparison of the strain energy at 0.10, 0.15, and 0.20 strain levels between the right side and the left side of the heart

Region	$W_{10\%}$				$W_{15\%}$				$W_{20\%}$			
	t	p	Cohen's d	Probability of superiority %	t	p	Cohen's d	Probability of superiority %	t	p	Cohen's d	Probability of superiority %
LV_{pooled} *vs.* RV_{pooled}	3.847	4.56 E-04	0.86	73.77	4.098	2.18 E-04	0.92	73.77	4.260	1.35 E-04	0.96	76.02
LA_{pooled} *vs.* RA_{pooled}	5.802	1.16 E-06	1.19	80.19	5.644	1.91 E-06	1.16	80.19	5.391	4.20 E-06	1.11	78.17
LAA vs. RAA	3.598	0.002	1.12	78.17	3.605	0.002	1.14	78.17	3.612	0.002	1.14	78.17

Lastly, comparison was made between the three anatomical regions on each side of the heart. One-way ANOVA test was performed to compare statistically the ventricle, atrium, and atrial appendage on each side of the heart. In this analysis, data from the anterior and posterior portions of the ventricles and atria were averaged into one representative data set for each region. One-way ANOVA revealed that there was a statistically significant difference in strain energy storage between the three anatomical regions of the left and right side of the heart at all the three strain levels (e.g. at 15% strain, left side: F=59.184; df= 2,54; p=2.54E-14, and right side: F= 70.327; df=2,54; p=9.215E-16). Note that the one-way ANOVA shows there is an overall difference between the regions, but ANOVA doesn't show which specific groups differ. In order to see where the difference occurs between the groups, the one-way ANOVA was followed by a Games Howell post hoc test and the results are summarized in Table 5-6. It was observed that in

all of the strain levels, strain energy storage differed significantly between each pair of the groups, with ventricle having the highest and atrium having the lowest values.

Table 5-6: Comparison of the strain energy at 0.10, 0.15, and 0.20 strain levels between the three regions on each side of the heart

	p value		
	$W_{10\%}$	$W_{15\%}$	$W_{20\%}$
$RV\ vs.\ RA$	6.49E-9	5.91E-9	5.47E-9
$RV\ vs.\ RAA$	4.08E-8	2.5E-8	1.35E-8
$RA\ vs.\ RAA$	0.029	0.034	0.042
$LV\ vs.\ LA$	9.02E-8	9.55E-8	3.76E-7
$LV\ vs.\ LAA$	1.27E-6	1.17E-6	3.68E-6
$LA\ vs.\ LAA$	0.003	0.003	0.003

Figure 5.3 provides a summary of the statistical analysis and shows the mean and standard deviation of strain energy storage at strain of 0.15. The results of t-test between the anterior and posterior portions of each region, and one-way ANOVA are represented in Figure 5.3a. Furthermore, the results of t-test between corresponding regions from the left and right sides of the heart at strain of 0.15 are summarized in Figure 5.3b. Moreover, the averaged Cauchy stress-Green strain curves are represented in Figure 5.4 and Figure 5.5 for anatomical regions of the left and right side of the heart, respectively. The error bars on the average curves represent standard deviation. The variations in the mechanical properties of the samples from the same location of the heart are due to the natural inter-subject differences. The maximum Coefficient of Variation (ratio of standard deviation to mean) for the left ventricle is 0.4 in the fiber direction and 0.5 in the cross fiber direction. Also for the right ventricle the maximum Coefficient of Variation is 0.4 both in the fiber and cross fiber directions. The Fung strain energy equation was also fitted to the averaged curves to determine the average material coefficients for each region. The coefficients are presented in Table 5-7.

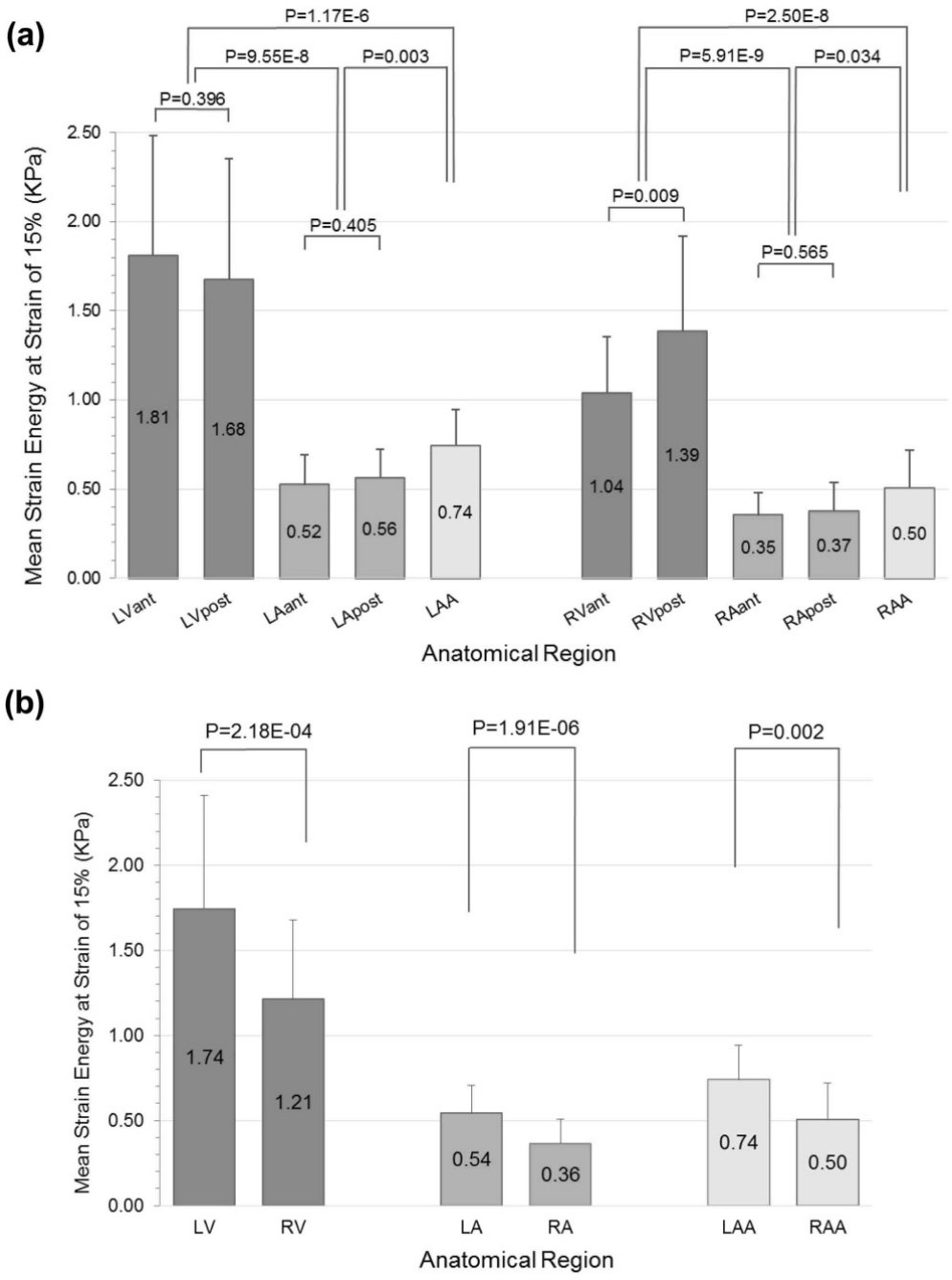

Figure 5.3: Mean values ± SD of strain energy storage at strain of 0.15. The results of t-test between the anterior and posterior portions of each region, and one-way ANOVA are represented in (a), and the results of t-test between corresponding regions from the left and right sides of the heart are summarized in (b).

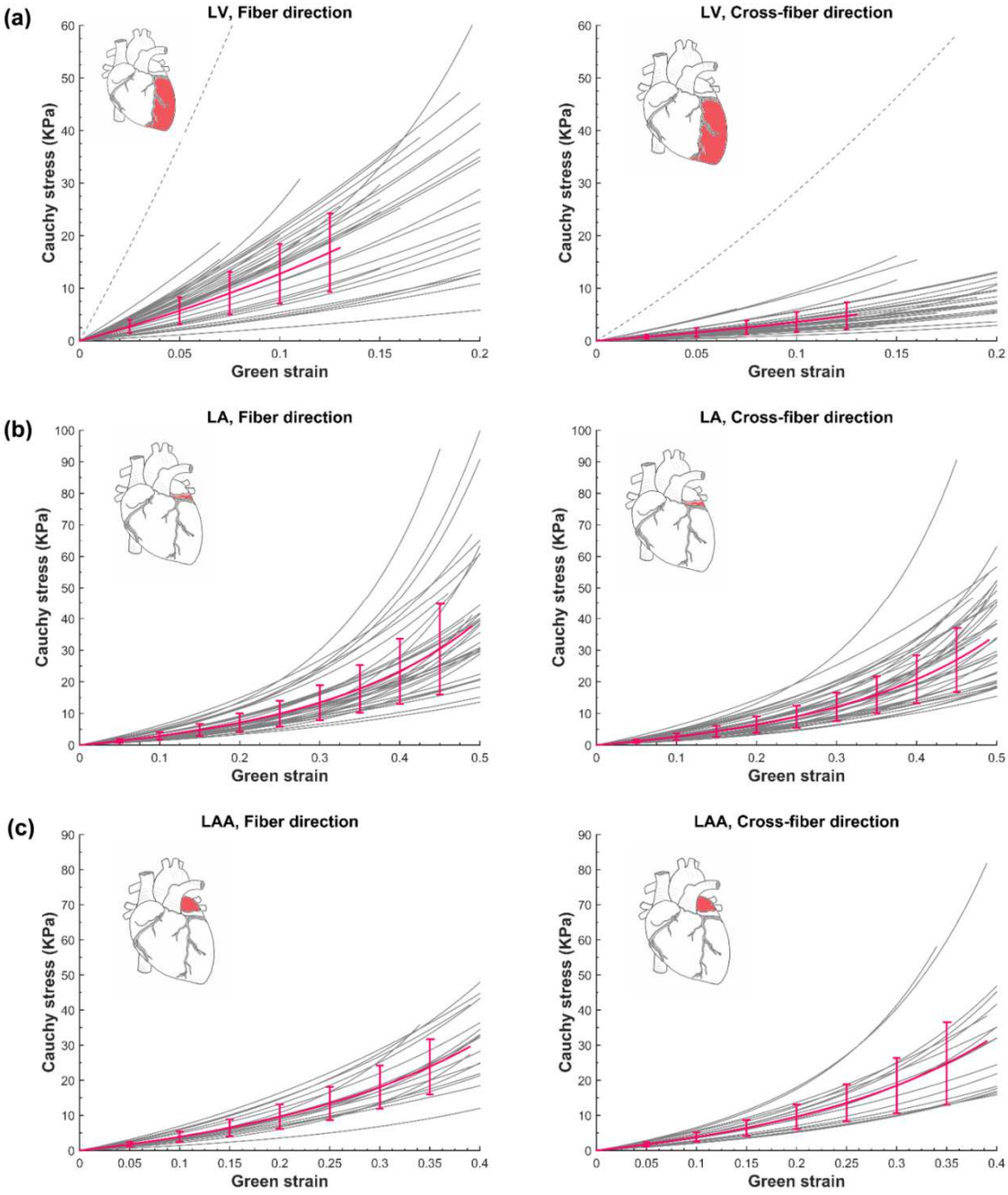

Figure 5.4: Equibiaxial stress-strain curves and the average curve for anatomical regions of the left side of the heart; (a) left ventricle, (b) left atrium, and (c) left atrial appendage. The error bars represent standard deviation. The graphs on each row are associated with the tissue specimen's main fiber direction (left) and cross fiber direction (right). The average curves were only extended to a strain level where actual experimental data were available for more than 80% of the samples. Samples which failed to stretch to that strain level were excluded from the average. The dashed line represents an outlier with stress values of greater than the average stress plus three times the standard deviation which was excluded from the average.

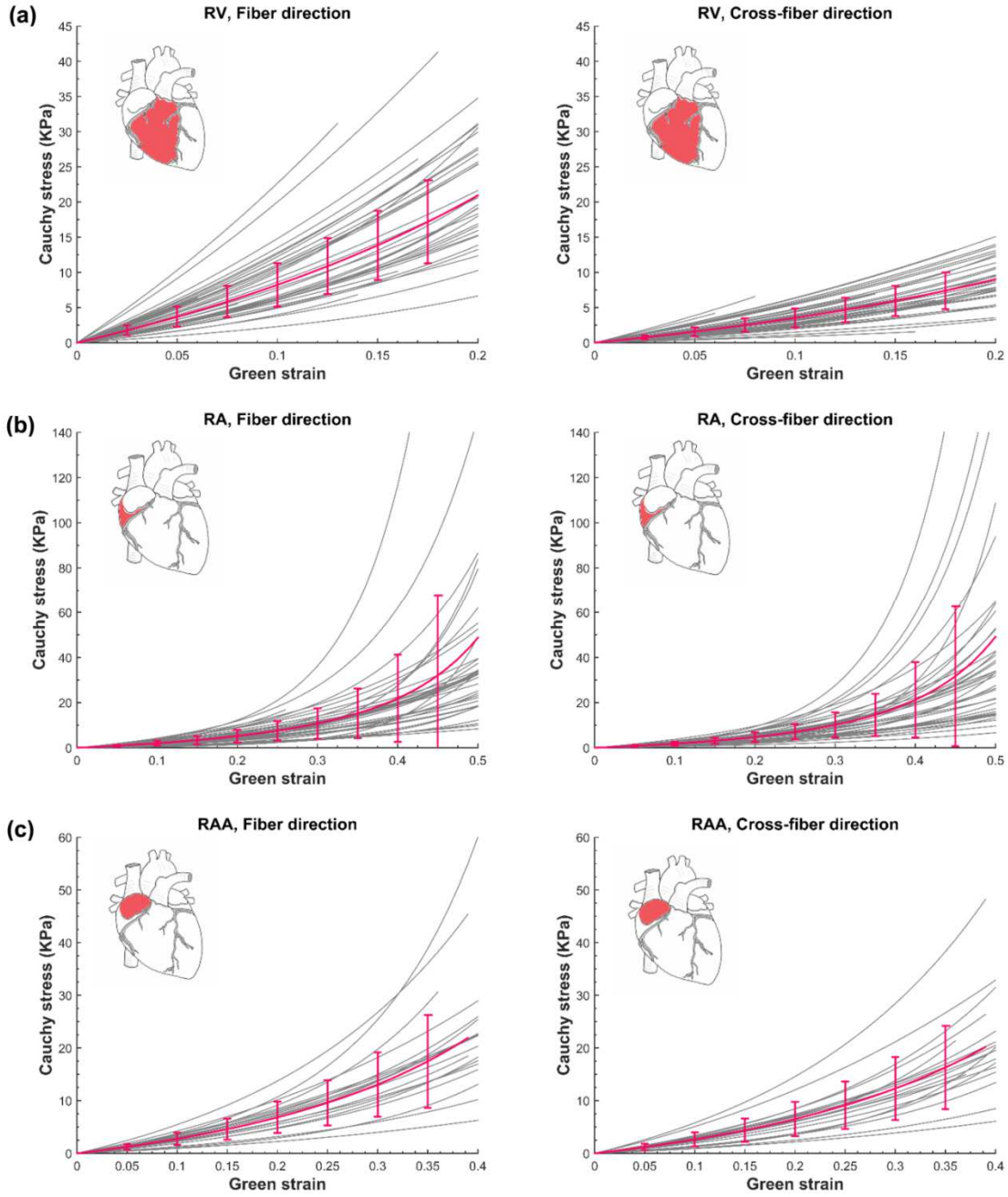

Figure 5.5: Equibiaxial stress-strain curves and the average curve for anatomical regions of the right side of the heart; (a) right ventricle, (b) right atrium, and (c) right atrial appendage. The error bars represent standard deviation. The graphs on each row are associated with the tissue specimen's main fiber direction (left) and cross fiber direction (right). The average curves were only extended to a strain level where actual experimental data were available for more than 80% of the samples. Samples which failed to stretch to that strain level were excluded from the average.

Table 5-7: Average constitutive coefficients of the four parameter Fung exponential model for the six anatomical regions of the healthy ovine heart

	c_{11}	c_{12}	c_{22}	C	RMS
LV	1.409	0.509	0.031	54.030	0.010
LA	0.125	0.978	0.005	21.101	0.111
RV	1.564	0.486	0.396	32.439	0.008
RA	1.114	1.430	1.082	5.367	0.500
LAA	1.037	0.022	1.070	29.220	0.173
RAA	1.087	0.017	1.017	20.441	0.085

Histological analysis was made on samples taken from the left and right ventricles, atria, and atrial appendages (Figure 5.6). Staining using Masson's trichrome stain effectively rendered myocytes red and collagen fibers light blue. In the ventricles, myofibers arranged themselves in a parallel orientation and changes in fiber direction were fairly smooth. While the atria and atrial appendages demonstrated rather abrupt changes in the fiber orientation and a less uniform fiber arrangement was observed in the tissues. The abrupt change of fiber angle is evident in the endocardial layer of the left atrium (Figure 5.6-III). The local variations in the atrial fiber orientation are attributed to the complex anatomical structure of the atria. Furthermore, the inner layer of the atria was covered with a thin collagenous layer (Figure 5.6-III and 5.6-VII). This collagenous layer plays a crucial role in the mechanical behavior of the atrial tissue[2]. Additionally, the appendages were trabeculated and lined by a collagenous surface. The interstices among myocytes in all of the regions were occupied by collagen fibers. More pictures of the histology samples is provided in appendix 2.

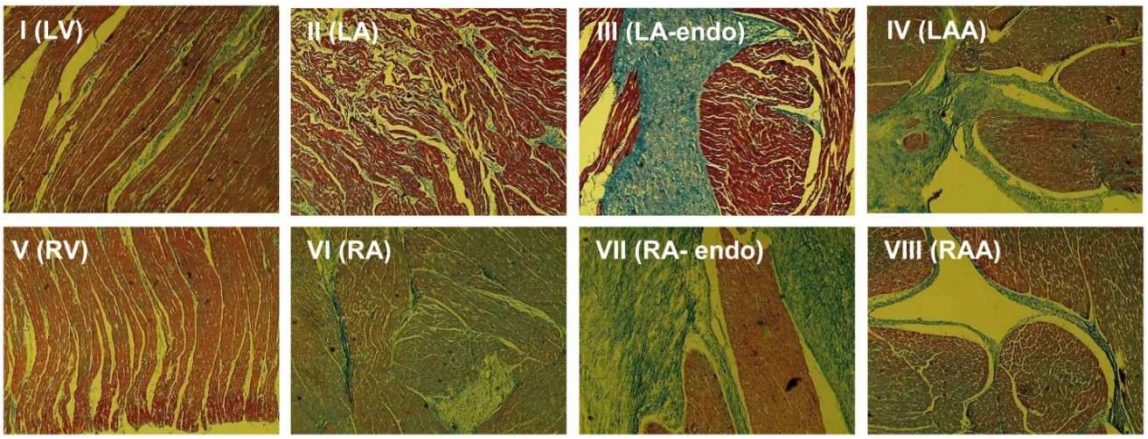

Figure 5.6: Masson's trichrome staining of (I) left ventricle, (II) left atrium, (III) endocardial layer of the left atrium, (IV) left atrial appendage, (V) right ventricle, (VI) right atrium, (VII) endocardial layer of the right atrium, and (VIII) right atrial appendage of the healthy ovine heart. Red: myocytes and light blue: collagen. The sections were observed at 4x magnification.

In addition, the average surface area ratio of collagen to myocyte was determined for each region and the results were summarized in Table 5-8. As expected, the internal surface of the atria had the highest amount of collagen compared to the other regions. Moreover, in each side of the heart, the surface area ratio of collagen to myocyte was lowest for the ventricles compared to atria and atrial appendages. This may explain the underlying basis for the fact that the ventricles were found to be significantly stiffer that atria and appendages. However, due to the small number of samples examined for the histological features of each region, no statistical analysis was performed. Further studies are needed to evaluate the correlation of microstructure and passive mechanical properties of the heart chambers.

Table 5-8: The average surface area ratio of collagen to myocyte for each anatomical region

	LV	*LA*	*LA_endo*	*LAA*	*RV*	*RA*	*RA_endo*	*RAA*
Collagen/Myocyte	0.13	0.34	0.66	0.35	0.10	0.13	0.52	0.18

CHAPTER 6: DISCUSSION

In this study, mechanical properties of ten different anatomical regions of ovine heart were determined by means of planar biaxial tests and a Fung-type strain energy function was used to fit the experimental data. The maximum stress value of the left ventricle in the fiber direction was about 18 Kpa when $E_{11} = 0.13$ (E_{11} being the normal stress in the fiber direction) which is comparable to the literature. Yin et al.[31] reported a fiber direction stress value of about 20kPa for dog hearts when $E_{11} \sim 0.2$. Sommer et al[25]. reported a fiber direction stress value of about 20 kPa when $E_{11} \sim 0.15$ for failed human hearts.

The stress–strain response of the tissue specimens were nonlinear both in fiber and cross-fiber directions. The nonlinearity was more pronounced in the atria and appendages than the ventricles. Nevertheless, the ventricles had the greatest slope of the stress-strain curves among all the regions. Furthermore, the ventricles had higher anisotropy than the other regions, with the left ventricle being the most anisotropic among all. In addition, tissue behavior was quantified based on the magnitude of strain energy function. A direct comparison was made between different anatomical regions at equibiaxial strains of 0.10, 0.15, and 0.20. Statistical analysis revealed no statistically significant difference in strain energy storage between the anterior and posterior regions of left atrium, right atrium, and left ventricle. However, strain energy stored in posterior specimens of the right ventricle was found to be significantly greater than that of the anterior specimens. Additionally, statistical analysis showed that all chambers

from the left side of the heart had significantly higher strain energy than the corresponding chambers on the right side of the heart at the three strain levels. Statistical comparison was also made between the three anatomical regions on each side of the heart, namely ventricle, atrium and the atrial appendage. Specimens from the ventricle were found to have the highest stiffness followed by specimens from the atrial appendage and lastly from the atrium. This trend was consistent in both sides of the heart.

The three common approaches employed for comparing tissue stiffness in the literature have been based on (i) the slope of the stress-strain curves, (ii) coefficients of the constitutive model, and (iii) magnitude of the stored strain energy. The main limitation of the first approach is that the slope of the stress-strain curves can provide a limited measure of tissue stiffness and it does not provide an overall assessment of stiffness. The slope of the stress-strain curve represents only one component of the elasticity tensor. The main limitation of the second approach is that the coefficients are highly sensitive to the curve fitting methodology as well as the initial estimate values. Therefore, the coefficients of constitutive model do not provide an accurate comparison of tissue mechanical behavior. On the other hand, the magnitude of strain energy function provides a simple and straightforward measure of the overall mechanical behavior of the soft tissue during deformation.

It is also important to highlight that curve averaging as opposed to coefficient averaging is the appropriate method to report the average mechanical response of soft tissue. Roberston et al.[24] demonstrated how average coefficients of constitutive models, as commonly reported in the field of biomedical material properties, fail to produce average mechanical responses and can generate non-physical results. Average nonlinear constitutive coefficients can produce non-average behaviors that are unrelated to the sample population from which the coefficients were derived. Therefore, in this study, averaged Cauchy stress-Green strain curves were obtained and

the Fung strain energy function was fitted to the averaged curves to determine the average material coefficients for each anatomical region. Furthermore, the individual coefficient set of each tissue specimen is reported in the Appendix 1.

In this comparative study, a four parameter Fung strain energy function was used to fit the experimental data. The model effectively captured the differences in the local mechanical properties of different anatomical regions. However, data from biaxial tests alone are not sufficient to fully characterize the passive response of the heart tissue[9]. The structure of myocardium is not transversely isotropic but orthotropic[9]. A combination of biaxial extension data and triaxial shear data at different orientations is required to capture the direction-dependent nonlinear anisotropic material response[9]. Recently, Sommer et al.[25] conducted biaxial extension and triaxial shear tests on human ventricular myocardium. Their study suggests that the passive human left ventricular myocardium exhibits nonlinear, orthotropic, viscoelastic, and history-dependent behavior. The experimental data can be fitted to Holzapfel-Ogden model or generalized Fung hyperelastic constitutive model for computational modeling. In addition to the experimental material characterization, mechanical properties of heart tissue can be estimated using a combination of magnetic resonance imaging, finite element modeling, and numerical optimization[18].

Pathological changes in the heart tissue due to various diseases greatly affect mechanical properties of heart tissue. A number of experimental studies have characterized the structural and functional changes that occur after cardiovascular diseases. For example, Gupta et al.[8] determined stiffness of infarcted and noninfarcted myocardia in sheep over a 64 day period. Equibiaxial stretching was performed on infarcted and remote tissue within 4 hours of the induction of myocardial infarction, as well as 1, 2, and 6 weeks. The results showed a significant increase in stiffness leading up to 2 weeks and then showed a significant decrease in stiffness at 6 weeks. In

another study, Hill et al.[17] studied the structural and mechanical adaptations of right ventricle free wall myocardium due to pulmonary hypertension in a rat model. Biaxial mechanical studies were performed on isolated myocardium obtained from normotensive and hypertensive hearts. An increase in both tissue stiffness and tissue anisotropy was observed in hypertensive rats. In addition, Bellini et al.[3] investigated and compared the passive mechanical response of atrial tissue at the healthy stage and the onset of atrial fibrillation in porcine specimens. An increase in tissue stiffness was observed after atrial fibrillation.

The results of this study are limited to the *in-vitro* setting. Residual stress was not considered in the constitutive modeling. Dissection of specimens from the heart chambers indeed released residual stresses that existed in the compound of the ventricles, atria, and appendages before specimen removal. Furthermore, the specimen may be damaged by ischemia or by calcium released from cells injured during sample excision. In addition, the deformations imposed by biaxial stretching differ from those experienced *in-vivo*. It is not possible to reproduce the *in-vivo* loading condition using the biaxial testing system. Nevertheless, the approach used in this study provided important data for biomechanical comparison of the heart chambers. Furthermore, in contrary to specimens excised from the atria and appendages which spanned the entire wall thickness, ventricular specimens were harvested only from myocardium. However, endocardium and epicardium play an important role in the mechanics of the ventricles as a whole. Another issue associated with the ventricular samples was that the fiber orientation varies through the thickness. The predominant muscle fiber direction rotates from $+50^{o}$ to $+70^{o}$ in sub-epicardial layer to nearly 0^{o} in the mid-wall region and finally to -50^{o} to -70^{o} in sub-endocardial layer[9]. Therefore, even in samples with an average thickness of 2 mm, the fiber angle gradient, although small, was notable. Finally, as noted earlier, data from biaxial tests alone are not sufficient to fully characterize the passive response of heart tissue. A combination of biaxial extension and

triaxial shear tests[25], or inverse finite element simulations[20] should be implemented to characterize the complete anisotropic behavior of soft tissue.

CHAPTER 7: CONCLUSION AND RECOMMENDATION

In conclusion, in the field of cardiovascular research, understanding the mechanical characterization of cardiac tissue is of utmost importance. For instance, in the design and development of many of the heart related therapies and devices such as the left atrial appendage closure devices, or tissue engineered cardiac patches, tissue mechanical properties play an important role. In this study, planar biaxial stretch testing was conducted on tissue specimens obtained from left and right ventricles, atria, and atrial appendages of healthy ovine hearts. Cauchy stress–Green strain curves were obtained for all the anatomical regions and a Fung-type constitutive model was used to fit the raw data. All the specimens exhibited nonlinear response to the biaxial loading, but the nonlinearity was more pronounced in the atria and atrial appendages than the ventricles. The ventricles however had higher tissue anisotropy than the other regions, with the left ventricle being the most anisotropic among all.

Furthermore, the anatomical regions were compared based on the magnitude of strain energy function at a wide range of strain levels. Statistical analysis revealed no statistically significant difference in strain energy storage between anterior and posterior portions of each anatomical region. The right ventricle was an exception where strain energy stored by posterior specimens was found to be statistically significantly greater than that stored by anterior specimens. Moreover, it was found that all chambers from the left side of the heart tend to be significantly stiffer than the corresponding chambers on the right side of the heart. Additionally, the three anatomical regions on each side of the heart were compared. It was observed that the

highest to lowest amount of strain energy were associated with ventricles, appendages, and atria, respectively. This trend was consistent in both sides of the heart.

Additionally, histological analysis revealed some of the tissue microstructural differences between different regions. Tissue specimens from different regions had different ratio of collagen to myocyte; with the atria having the highest and ventricles having the lowest. Considering the fact that the amount of collagen in the tissue is one of the factors that contributes to the tissue compliance, some of the differences between the mechanical responses of different regions could be explained. In this light, the results of histology were consistent with the findings of the biaxial testing.

Overall, in the field of heart research, understanding the mechanical properties of the cardiac tissue plays a crucial role. Whether the goal is to merely understand a disease condition and how it impacts the heart, or to develop a new therapy, the tissue mechanical properties always come into play. Moreover, it is important to realize that although all of the heart chamber are from the same embryonic origin, their mechanical behavior alters through the heart development. To the best of our knowledge, this was the first comprehensive study that compared the mechanical behavior of all anatomical regions of the heart. Also, limited data was available on the mechanical properties of the atrial appendages.

The future direction of the study of mechanics of cardiac tissue would be to conduct triaxial testing, rather than biaxial. Although biaxial testing provides valuable information about the tissue behavior, and could be particularly useful when comparing the mechanical response of different tissues, it is limited to the in-plane loading configuration. Therefore, only a 2D constitutive model can be obtained from the biaxial experimental data. While, for finite element analysis of the heart, a complete set of 3D material coefficients is needed. To our knowledge, there is no triaxial test equipment to date due to technical challenges.

Additionally, when working with any biological material such as soft tissue, there are always variations to the experimental data due to the natural inter-subject differences in the mechanical response of the material. In this case, although the best practice is to use subject-specific material properties in biomechanics investigations, it is not always practical. Therefore, a probabilistic approach is recommended to characterize the inter-subject variability in the mechanical properties of the material. This approach enables us to investigate the impact of inter-subject variability on model outputs[32].

REFERENCES

1. Abbasi M. and A. N. Azadani. Leaflet stress and strain distributions following incomplete transcatheter aortic valve expansion. *J Biomech* 48: 3663-3671, 2015.

2. Bellini C. Mechanical Behaviour of the Human Atria. *Annals of Biomedical Engineering* 2012.

3. Bellini C. and E. S. Di Martino. A mechanical characterization of the porcine atria at the healthy stage and after ventricular tachypacing. *J Biomech Eng* 134: 021008, 2012.

4. Bers D. M. Cardiac excitation–contraction coupling. *Nature* 415: 198-205, 2002.

5. Fung Y., K. Fronek and P. Patitucci. Pseudoelasticity of arteries and the choice of its mathematical expression. *American Journal of Physiology-Heart and Circulatory Physiology* 237: H620-H631, 1979.

6. Genet M., L. C. Lee, R. Nguyen, H. Haraldsson, G. Acevedo-Bolton, Z. Zhang, L. Ge, K. Ordovas, S. Kozerke and J. M. Guccione. Distribution of normal human left ventricular myofiber stress at end diastole and end systole: a target for in silico design of heart failure treatments. *Journal of Applied Physiology* 117: 142-152, 2014.

7. Grossman W. Cardiac hypertrophy: useful adaptation or pathologic process? *The American journal of medicine* 69: 576-584, 1980.

8. Gupta K. B., M. B. Ratcliffe, M. A. Fallert, L. H. Edmunds, Jr. and D. K. Bogen. Changes in passive mechanical stiffness of myocardial tissue with aneurysm formation. *Circulation* 89: 2315-2326, 1994.

9. Holzapfel G. A. and R. W. Ogden. Constitutive modelling of passive myocardium: a structurally based framework for material characterization. *Philos Trans A Math Phys Eng Sci* 367: 3445-3475, 2009.

10. Huang, Y., O. Kawaguchi, B. Zeng, R. A. Carrington, C. J. Horam, T. Yuasa, N. Abdul-Hussein, and S. N. Hunyor. A Stable Ovine Congestive Heart Failure Model A Suitable Substrate for Left Ventricular Assist Device Assessment. 1997.

11. Jennifer A. Dixon M. F. G. S., MD, PhD. Large Animal Models of Heart Failure A Critical Link in the Translation of Basic Science to Clinical Practice. 2009.

12. Kindberg K., H. Haraldsson, A. Sigfridsson, J. Engvall, N. B. Ingels, T. Ebbers and M. Karlsson. Myocardial strains from 3D displacement encoded magnetic resonance imaging. *BMC medical imaging* 12: 9, 2012.

13. Kohl P., P. Hunter and D. Noble. Stretch-induced changes in heart rate and rhythm: clinical observations, experiments and mathematical models. *Progress in biophysics and molecular biology* 71: 91-138, 1999.

14. Kourliouros A., I. Savelieva, A. Kiotsekoglou, M. Jahangiri and J. Camm. Current concepts in the pathogenesis of atrial fibrillation. *American heart journal* 157: 243-252, 2009.

15. Lee L. C., S. T. Wall, D. Klepach, L. Ge, Z. Zhang, R. J. Lee, A. Hinson, J. H. Gorman, R. C. Gorman and J. M. Guccione. Algisyl-LVR™ with coronary artery bypass grafting reduces left ventricular wall stress and improves function in the failing human heart. *International journal of cardiology* 168: 2022-2028, 2013.

16. Leor J., S. Aboulafia-Etzion, A. Dar, L. Shapiro, I. M. Barbash, A. Battler, Y. Granot and S. Cohen. Bioengineered cardiac grafts: A new approach to repair the infarcted myocardium? *Circulation* 102: III56-61, 2000.

17. Michael R. Hill M. A. S., Daniela Valdez-Jasso, Will Zhang, Hunter C. Champion, Michael S. Sacks. Structural and Mechanical Adaptations of Right Ventricle Free Wall Myocardium to Pressure Overload. 2014.

18. Mojsejenko D., J. R. McGarvey, S. M. Dorsey, J. H. Gorman III, J. A. Burdick, J. J. Pilla, R. C. Gorman and J. F. Wenk. Estimating passive mechanical properties in a myocardial infarction using MRI and finite element simulations. *Biomechanics and modeling in mechanobiology* 14: 633-647, 2014.

19. Moorman A., S. Webb, N. A. Brown, W. Lamers and R. H. Anderson. Development of the heart:(1) formation of the cardiac chambers and arterial trunks. *Heart* 89: 806-814, 2003.

20. Nikou A., S. M. Dorsey, J. R. McGarvey, J. H. Gorman III, J. A. Burdick, J. J. Pilla, R. C. Gorman and J. F. Wenk. Computational Modeling of Healthy Myocardium in Diastole. *Ann Biomed Eng* 1-13, 2015.

21. Quinn T. A. The importance of non-uniformities in mechano-electric coupling for ventricular arrhythmias. *Journal of Interventional Cardiac Electrophysiology* 39: 25-35, 2014.

22. Ravens U. Mechano-electric feedback and arrhythmias. *Progress in biophysics and molecular biology* 82: 255-266, 2003.

23. Robertson D. and D. Cook. Unrealistic statistics: How average constitutive coefficients can produce non-physical results. *J Mech Behav Biomed Mater* 40: 234-239, 2014.

24. Robertson D. and D. Cook. Unrealistic statistics: how average constitutive coefficients can produce non-physical results. *J Mech Behav Biomed Mater* 40: 234-239, 2014.

25. Sommer G., A. J. Schriefl, M. Andrä, M. Sacherer, C. Viertler, H. Wolinski and G. A. Holzapfel. Biomechanical properties and microstructure of human ventricular myocardium. *Acta biomaterialia* 24: 172-192, 2015.

26. Sylva M., M. J. van den Hoff and A. F. Moorman. Development of the human heart. *American Journal of Medical Genetics Part A* 164: 1347-1371, 2014.

27. Voelkel N. F., R. A. Quaife, L. A. Leinwand, R. J. Barst, M. D. McGoon, D. R. Meldrum, J. Dupuis, C. S. Long, L. J. Rubin, F. W. Smart, Y. J. Suzuki, M. Gladwin, E. M. Denholm, D. B. Gail, L. National Heart, C. Blood Institute Working Group on and F. Molecular Mechanisms of Right Heart. Right ventricular function and failure: report of a National Heart, Lung, and Blood Institute working group on cellular and molecular mechanisms of right heart failure. *Circulation* 114: 1883-1891, 2006.

28. Wang B., A. Borazjani, M. Tahai, A. L. de Jongh Curry, D. T. Simionescu, J. Guan, F. To, S. H. Elder and J. Liao. Fabrication of cardiac patch with decellularized porcine myocardial scaffold and bone marrow mononuclear cells. *Journal of Biomedical Materials Research Part A* 94: 1100-1110, 2010.

29. Wang F. and J. Guan. Cellular cardiomyoplasty and cardiac tissue engineering for myocardial therapy. *Advanced drug delivery reviews* 62: 784-797, 2010.

30. Habets, P. E. M. H., Moorman, A. F. M., Clout, D. E. W., van Roon, M.A., Lingbeek, M., van Lohuizen, M., Campione, M. and Christoffels, V. M. Heart Development, 2002.

31. Frank C.P., R. K. Strumpf, P. H. Chew, S. L. Zeger. Quantification of the mechanical properties of noncontracting canine myocardium under simultaneous biaxial loading. *Journal of Biomechanics,* 1987.

APPENDIX 1

The individual coefficient sets of the four parameter Fung exponential constitutive model for all of the individual hearts (n=19). Furthermore, the maximum Green strain values reached in the biaxial tests were shown in the table.

	Region	$\mathbf{c_{11}}$	$\mathbf{c_{12}}$	$\mathbf{c_{22}}$	**C**	**RMS**	**Maximum Strain**	
							Fiber	**Cross-fiber**
1	LV_{ant}	0.67	1.48	0.00	25.09	2.18	0.39	0.25
	LV_{post}	0.02	0.00	0.04	1048.12	1.82	0.61	0.41
	LA_{ant}	0.00	0.25	0.09	52.20	2.24	0.77	1.27
	LA_{post}	0.00	0.07	0.00	270.23	1.33	0.70	1.20
	LAA	0.05	0.02	0.04	363.99	2.96	0.94	1.46
	RV_{ant}	0.16	0.17	0.00	163.53	1.30	0.20	0.40
	RV_{post}	0.04	0.00	0.01	2534.15	4.30	0.41	1.11
	RA_{ant}	0.00	0.29	0.34	27.47	0.80	0.57	0.69
	RA_{post}	0.00	1.30	0.81	4.00	4.22	0.82	0.85
	RAA	0.11	0.09	0.21	143.18	1.55	0.78	0.47
2	LV_{ant}	0.22	0.49	0.00	52.61	1.53	0.31	0.51
	LV_{post}	4.29	0.33	0.73	7.87	0.88	0.27	0.34
	LA_{ant}	1.44	0.00	0.88	11.90	1.85	0.60	0.67
	LA_{post}	0.00	0.27	0.12	43.30	0.66	0.64	0.77
	LAA	0.96	0.52	0.00	32.57	3.50	0.59	0.73
	RV_{ant}	0.03	0.02	0.01	883.80	1.32	0.27	0.47
	RV_{post}	1.05	0.00	0.21	82.38	1.19	0.21	0.47
	RA_{ant}	0.67	0.38	0.28	6.67	0.79	0.75	0.91
	RA_{post}	0.00	0.86	0.15	13.55	4.29	0.69	0.83
	RAA	0.10	0.04	0.06	203.54	1.13	0.70	0.48
3	LV_{ant}	0.88	0.00	0.18	160.51	2.47	0.23	0.41
	LV_{post}	0.05	0.01	0.01	1653.03	2.09	0.25	0.42
	LA_{ant}	0.04	1.72	0.00	6.87	2.20	0.58	0.61
	LA_{post}	0.52	0.65	0.00	17.70	1.08	0.58	0.61
	LAA	0.08	0.40	0.00	55.67	1.13	0.73	0.50
	RV_{ant}	1.74	0.36	0.47	47.08	2.49	0.24	0.49
	RV_{post}	0.04	0.06	0.00	770.25	1.32	0.37	0.33
	RA_{ant}	0.11	0.68	0.69	13.61	1.51	0.59	0.64
	RA_{post}	0.00	2.77	3.15	3.46	6.17	0.52	0.49
	RAA	0.10	0.31	0.08	62.02	1.08	0.75	0.60

	Region	c_{11}	c_{12}	c_{22}	C	RMS	Maximum Strain	
							Fiber	Cross-fiber
4	LV_{ant}	3.11	0.25	0.73	17.35	1.38	0.27	0.45
	LV_{post}	3.92	0.00	1.54	9.93	1.79	0.30	0.42
	LA_{ant}	0.00	1.29	0.33	15.47	2.27	0.65	0.62
	LA_{post}	0.00	0.12	0.21	150.97	1.58	0.78	0.70
	LAA	0.00	0.92	0.43	12.69	2.13	0.62	0.70
	RV_{ant}	5.53	0.00	2.46	8.99	1.49	0.24	0.36
	RV_{post}	0.20	0.00	0.05	523.11	2.06	0.27	0.48
	RA_{ant}	0.95	0.76	0.00	10.34	1.98	0.66	0.69
	RA_{post}	0.26	0.71	0.00	13.96	1.31	0.67	0.78
	RAA	0.00	0.02	0.49	13.95	0.63	0.70	0.84
5	LV_{ant}	0.21	0.00	0.06	592.22	1.69	0.20	0.32
	LV_{post}	13.73	0.27	2.08	8.36	1.46	0.13	0.30
	LA_{ant}	1.29	1.23	0.00	14.06	5.55	0.54	0.80
	LA_{post}	0.00	0.17	0.12	120.58	1.83	0.69	0.62
	LAA	0.20	0.67	0.00	35.16	1.39	0.53	0.65
	RV_{ant}	0.08	0.01	0.03	734.75	0.65	0.20	0.33
	RV_{post}	0.10	0.06	0.01	770.97	1.50	0.22	0.42
	RA_{ant}	0.07	1.59	0.00	10.49	7.80	0.77	0.64
	RA_{post}	1.85	0.75	0.00	11.75	1.48	0.57	0.61
	RAA	1.92	0.81	1.10	9.89	0.88	0.45	0.37
6	LV_{ant}	0.31	0.11	0.03	553.86	2.34	0.07	0.32
	LV_{post}	0.11	0.00	0.02	1651.87	2.96	0.19	0.38
	LA_{ant}	0.06	0.44	0.00	32.63	1.17	0.63	0.61
	LA_{post}	0.00	0.42	0.18	38.89	0.76	0.61	0.51
	LAA							
	RV_{ant}	1.62	2.08	0.14	15.90	1.59	0.25	0.41
	RV_{post}	0.55	0.28	0.07	110.14	1.95	0.21	0.43
	RA_{ant}	0.88	0.28	0.62	28.71	2.60	0.76	0.65
	RA_{post}	1.30	2.30	0.00	9.29	10.32	0.56	0.58
	RAA	0.62	0.62	0.70	35.59	1.32	0.44	0.40
7	LV_{ant}	1.52	0.48	0.55	33.17	1.23	0.26	0.39
	LV_{post}	0.24	0.00	0.07	184.00	0.78	0.20	0.44
	LA_{ant}	2.51	0.00	1.58	14.32	2.25	0.52	0.56
	LA_{post}	0.00	0.38	0.21	60.96	1.20	0.65	0.73
	LAA	0.24	0.04	0.18	208.90	1.45	0.64	0.64
	RV_{ant}	0.12	0.33	0.00	156.10	1.52	0.28	0.43
	RV_{post}	0.36	0.11	0.13	204.37	2.83	0.31	0.44
	RA_{ant}	0.00	2.60	0.24	4.79	4.90	0.60	0.60
	RA_{post}	0.00	2.18	1.99	3.13	3.59	0.62	0.53
	RAA	0.46	0.03	0.33	72.74	1.23	0.68	0.77

	Region	c_{11}	c_{12}	c_{22}	C	RMS	Maximum Strain	
							Fiber	Cross-fiber
8	LV_{ant}	0.00	2.82	0.50	21.66	1.89	0.15	0.30
	LV_{post}	24.68	0.00	2.82	6.66	1.50	0.11	0.34
	LA_{ant}	0.18	0.58	0.12	37.98	1.20	0.56	0.78
	LA_{post}	1.04	1.32	0.00	10.23	1.57	0.52	0.59
	LAA	0.00	1.70	0.03	16.31	1.28	0.41	0.55
	RV_{ant}	5.49	1.78	0.00	10.44	2.05	0.20	0.38
	RV_{post}	3.89	2.61	0.00	7.51	1.70	0.21	0.40
	RA_{ant}	1.77	2.47	0.19	6.30	0.70	0.27	0.52
	RA_{post}	1.08	0.67	1.14	8.75	0.63	0.27	0.40
	RAA	2.02	0.00	2.65	4.26	0.61	0.52	0.43
9	LV_{ant}	0.05	0.02	0.00	1579.22	2.60	0.26	0.47
	LV_{post}	0.01	0.02	0.00	3492.16	3.55	0.16	0.44
	LA_{ant}	0.76	0.10	0.19	53.37	1.28	0.52	0.81
	LA_{post}	0.02	0.12	0.19	132.66	1.18	0.69	0.61
	LAA	0.15	0.15	0.15	102.76	1.44	0.68	0.73
	RV_{ant}	1.34	0.77	0.50	23.56	0.74	0.34	0.41
	RV_{post}	0.31	0.08	0.04	427.42	3.14	1.38	0.18
	RA_{ant}	0.91	0.48	0.27	13.62	1.43	0.72	0.85
	RA_{post}	0.12	0.48	0.04	49.53	3.33	0.66	0.82
	RAA	0.14	0.23	0.22	56.38	0.81	0.69	0.69
10	LV_{ant}	8.83	1.08	2.78	11.26	1.68	0.15	0.24
	LV_{post}	6.86	0.32	0.62	17.75	0.62	0.11	0.29
	LA_{ant}	3.02	0.00	2.43	5.37	2.13	0.50	0.55
	LA_{post}	0.09	2.45	0.00	15.70	5.73	0.52	0.45
	LAA	0.00	1.32	0.35	21.58	3.34	0.49	0.65
	RV_{ant}	0.00	2.47	0.05	12.18	1.43	0.31	0.40
	RV_{post}	2.47	2.40	0.00	3.64	0.65	0.30	0.37
	RA_{ant}	0.49	0.50	0.62	13.83	0.83	0.57	0.59
	RA_{post}	2.59	0.00	2.19	7.26	1.99	0.51	0.55
	RAA	0.04	0.81	0.41	22.68	0.83	0.39	0.43
11	LV_{ant}	4.67	0.00	0.67	23.88	1.18	0.15	0.39
	LV_{post}	15.17	0.00	2.69	9.21	1.65	0.10	0.30
	LA_{ant}	1.04	0.00	0.66	36.73	0.71	0.46	0.53
	LA_{post}	0.58	0.18	0.48	40.04	0.72	0.49	0.48
	LAA	0.00	1.35	2.69	12.84	5.44	0.39	0.49
	RV_{ant}	0.40	0.00	0.11	223.74	1.49	0.23	0.33
	RV_{post}	4.70	0.00	1.92	11.12	1.70	0.26	0.37
	RA_{ant}	0.03	0.14	0.15	43.38	0.76	0.50	0.60
	RA_{post}	1.47	4.71	0.00	4.57	3.36	0.39	0.45
	RAA	1.43	0.00	0.77	10.84	0.53	0.42	0.64

	Region	c_{11}	c_{12}	c_{22}	C	RMS	Maximum Strain	
							Fiber	Cross-fiber
12	LV_{ant}	31.18	0.00	1.36	4.86	1.36	0.07	0.39
	LV_{post}	0.00	13.19	2.97	4.54	1.12	0.01	0.24
	LA_{ant}	0.00	0.51	0.39	41.73	1.17	0.47	0.54
	LA_{post}	0.55	0.12	0.15	76.24	1.13	0.54	0.68
	LAA	0.53	0.21	0.44	55.12	1.09	0.44	0.57
	RV_{ant}	0.07	0.07	0.00	658.70	1.17	0.22	0.29
	RV_{post}	0.00	0.48	0.09	123.93	2.15	0.08	0.38
	RA_{ant}	0.00	1.04	0.94	15.33	1.83	0.49	0.52
	RA_{post}	0.00	2.78	2.58	3.73	4.22	0.52	0.49
	RAA	0.69	0.33	0.44	23.79	0.81	0.37	0.59
13	LV_{ant}	0.28	0.04	0.01	475.68	1.34	0.13	0.36
	LV_{post}	3.99	0.70	0.10	35.20	1.33	0.10	0.37
	LA_{ant}	0.00	0.87	0.10	25.78	1.79	0.59	0.65
	LA_{post}	0.38	0.05	0.35	58.13	0.77	0.52	0.49
	LAA	0.35	0.21	0.31	91.46	1.36	0.42	0.47
	RV_{ant}	0.24	0.00	0.04	200.61	0.52	0.16	0.28
	RV_{post}	0.07	0.10	0.01	551.19	0.99	0.06	0.33
	RA_{ant}	0.54	0.00	0.23	42.96	1.27	0.62	0.71
	RA_{post}	0.74	0.00	0.49	22.14	0.70	0.56	0.61
	RAA	0.30	0.42	0.67	14.64	0.52	0.47	0.43
14	LV_{ant}	0.21	0.00	0.03	579.99	1.10	0.14	0.37
	LV_{post}	0.72	0.00	0.12	175.17	1.74	0.20	0.36
	LA_{ant}	0.00	1.70	0.64	8.11	1.42	0.60	0.52
	LA_{post}	0.71	0.01	0.27	42.22	0.85	0.50	0.57
	LAA	0.46	0.24	0.30	34.54	0.83	0.56	0.57
	RV_{ant}	0.97	1.68	0.00	19.15	1.63	0.31	0.34
	RV_{post}	0.96	0.00	0.09	194.57	1.41	0.13	0.35
	RA_{ant}	0.96	0.00	0.28	25.01	1.38	0.60	0.68
	RA_{post}	0.27	0.76	0.26	19.40	1.78	0.61	0.64
	RAA	0.26	0.42	0.12	37.91	0.79	0.48	0.51
15	LV_{ant}	2.01	0.00	0.50	46.41	1.45	0.23	0.31
	LV_{post}	0.82	0.00	0.09	210.85	1.62	0.16	0.32
	LA_{ant}	0.24	1.07	0.00	29.54	2.00	0.53	0.49
	LA_{post}	0.30	0.27	0.15	42.46	0.69	0.52	0.62
	LAA	1.49	0.00	2.06	17.31	1.17	0.51	0.44
	RV_{ant}	2.75	2.57	0.25	8.71	1.40	0.27	0.41
	RV_{post}	0.99	0.34	0.03	77.94	1.44	0.20	0.38
	RA_{ant}	0.67	0.00	0.30	40.01	0.61	0.52	0.55
	RA_{post}	0.80	0.76	0.00	18.87	1.17	0.53	0.58
	RAA	0.20	0.88	0.09	24.05	0.75	0.45	0.43

	Region	c_{11}	c_{12}	c_{22}	C	RMS	Maximum Strain	
							Fiber	Cross-fiber
16	LV_{ant}	0.18	0.00	0.02	931.36	2.29	0.17	0.33
	LV_{post}	0.08	0.00	0.01	1699.92	2.46	0.15	0.32
	LA_{ant}	0.00	1.18	0.14	13.52	1.41	0.67	0.51
	LA_{post}	0.45	0.49	0.00	32.67	1.11	0.57	0.61
	LAA	0.30	0.85	0.00	38.22	1.34	0.50	0.57
	RV_{ant}	0.78	0.00	0.18	143.18	0.81	0.17	0.36
	RV_{post}	2.74	2.02	0.00	16.78	1.22	0.14	0.34
	RA_{ant}	1.46	0.00	3.39	3.71	0.67	0.57	0.53
	RA_{post}	1.03	0.00	1.06	19.02	0.95	0.44	0.38
	RAA	0.47	0.40	0.57	20.94	0.81	0.54	0.49
17	LV_{ant}	0.10	0.05	0.00	4493.82	12.61	0.18	0.37
	LV_{post}	0.09	0.00	0.01	1838.03	3.48	0.19	0.46
	LA_{ant}	0.00	2.12	0.25	6.78	1.47	0.55	0.49
	LA_{post}	0.38	0.29	0.09	45.61	0.78	0.54	0.60
	LAA	1.00	0.00	0.99	32.71	1.01	0.52	0.56
	RV_{ant}	3.85	0.00	1.49	10.38	1.52	0.32	0.54
	RV_{post}	0.24	0.00	0.03	411.60	1.53	0.27	0.45
	RA_{ant}	0.95	1.06	0.00	5.82	0.91	0.58	0.61
	RA_{post}	0.00	3.45	4.18	0.90	5.06	0.54	0.51
	RAA	0.00	1.37	0.33	15.73	1.02	0.40	0.52
18	LV_{ant}	0.07	0.00	0.01	2211.84	3.10	0.18	0.45
	LV_{post}	0.03	0.02	0.00	1678.98	1.46	0.34	0.40
	LA_{ant}	0.00	0.90	0.22	26.26	2.70	0.72	0.62
	LA_{post}	0.02	0.40	0.00	58.14	0.69	0.51	0.55
	LAA	1.08	0.00	2.03	19.41	2.26	0.59	0.40
	RV_{ant}	0.51	0.83	0.00	37.12	1.57	0.41	0.50
	RV_{post}	2.23	1.08	0.39	14.78	2.01	0.32	0.54
	RA_{ant}	1.26	0.00	0.65	15.24	0.90	0.55	0.58
	RA_{post}	0.00	1.72	0.25	5.59	2.49	0.68	0.52
	RAA	0.48	1.33	0.00	8.45	0.64	0.44	0.50
19	LV_{ant}	14.95	0.68	1.17	11.41	2.13	0.07	0.41
	LV_{post}	0.00	5.48	1.49	7.16	1.83	0.04	0.35
	LA_{ant}	0.00	0.75	0.43	28.84	1.04	0.43	0.54
	LA_{post}	0.00	1.53	0.27	11.00	2.59	0.53	0.67
	LAA	0.00	2.46	1.53	12.08	3.07	0.34	0.42
	RV_{ant}	3.05	5.77	0.00	3.25	0.94	0.14	0.36
	RV_{post}	2.53	0.57	1.21	12.58	0.85	0.21	0.35
	RA_{ant}	0.52	1.12	0.83	8.54	0.68	0.56	0.55
	RA_{post}	0.00	2.08	1.66	2.08	2.51	0.63	0.56
	RAA	3.23	1.63	0.00	6.06	2.18	0.46	0.46

APPENDIX 2

Masson's trichrome staining of tissue samples from left ventricle, left atrium, endocardial layer of the left atrium, left atrial appendage, right ventricle, right atrium, endocardial layer of the right atrium, and right atrial appendage of the healthy ovine heart. Red: myocytes are rendered red and collagen fibers are rendered blue. The sections were observed at 4x magnification.

2.1: Left ventricle

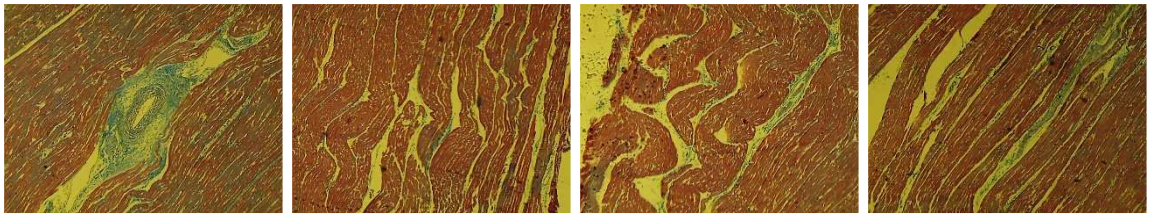

2.2: Left atrium

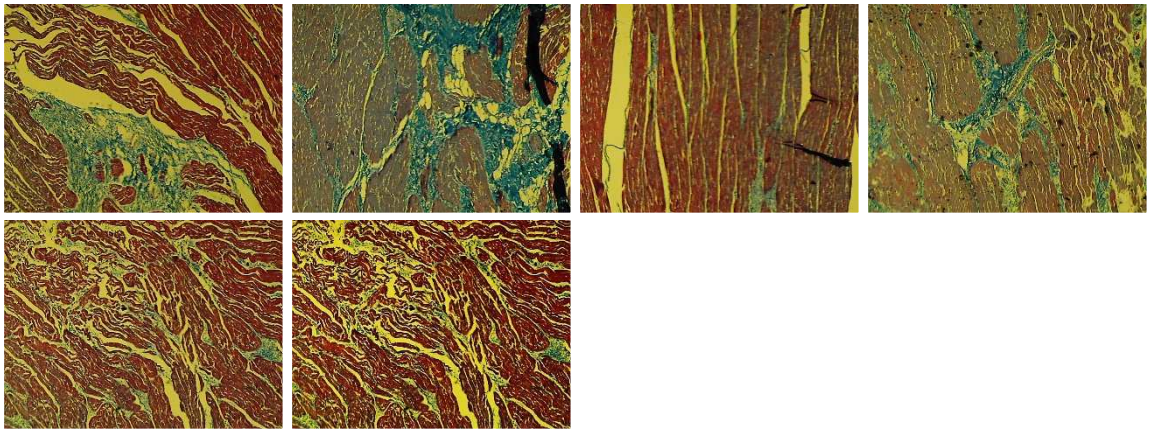

2.3 Endocardial layer of the left atrium

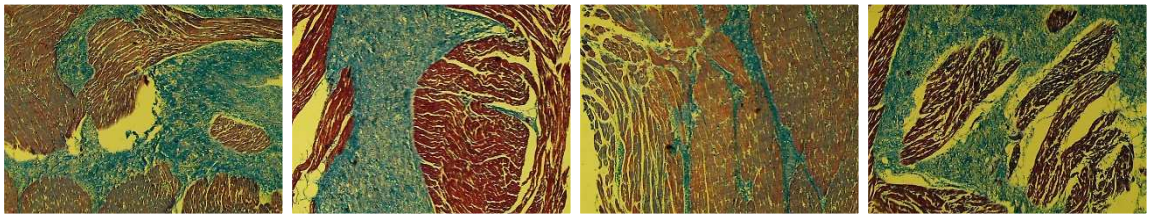

2.4: Left atrial appendage

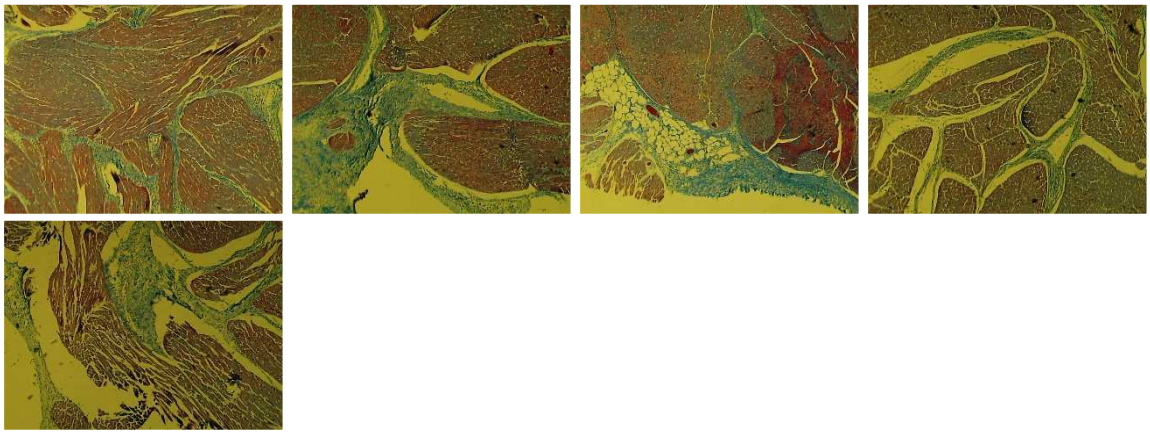

2.5: Right Ventricle

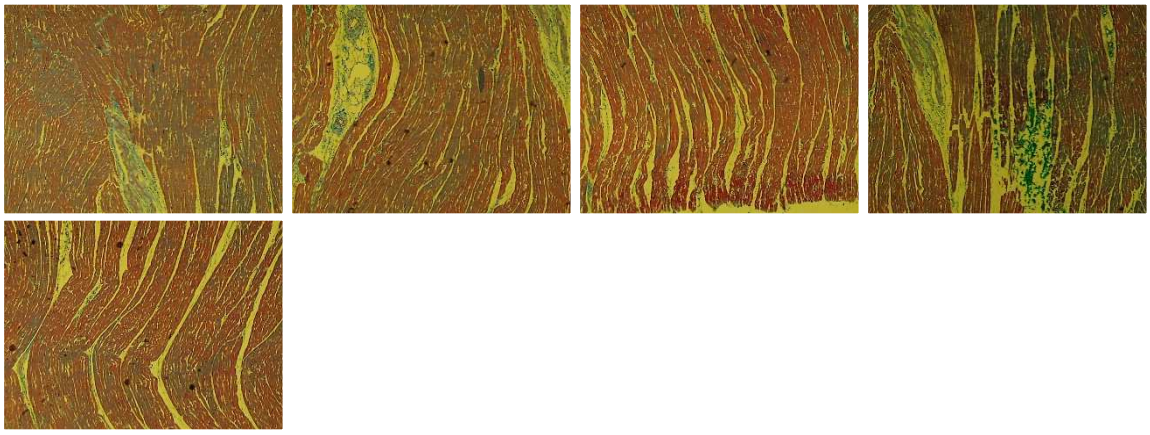

2.6: Right atrium

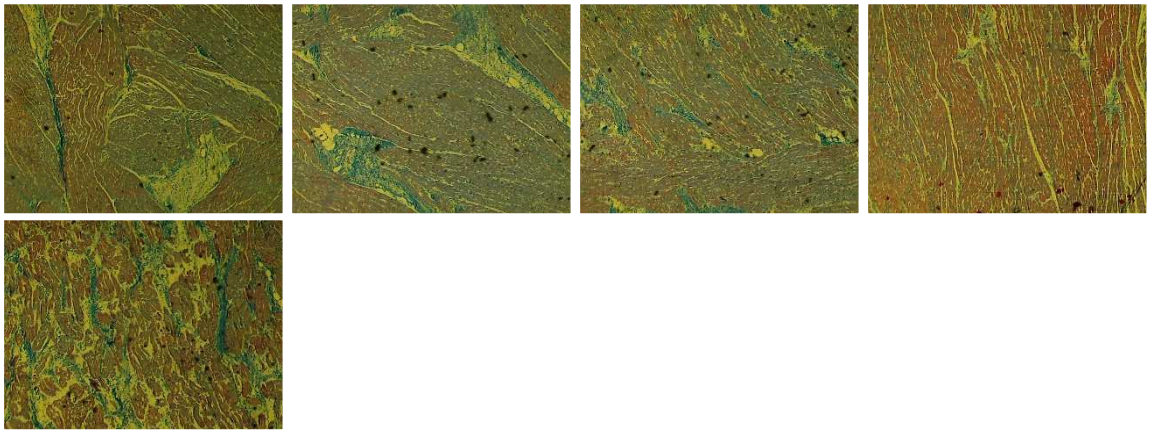

2.7: Endocardial layer of the right atrium

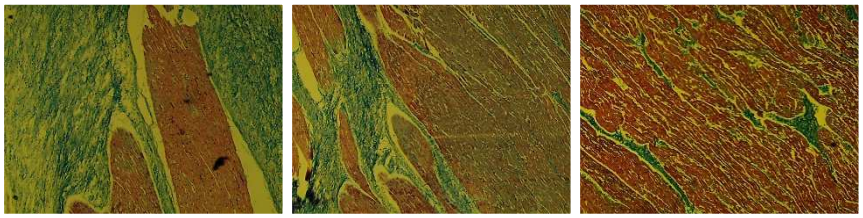

2.8: Right atrial appendage